Alpine rock glacier activity over Holocene to modern timescales (western French Alps)

Benjamin Lehmann[1,2*], Robert S. Anderson[2], Xavier Bodin[1], Diego Cusicanqui[1,3], Pierre G. Valla[4], and Julien Carcaillet[4]

[1]Université Savoie Mont Blanc, CNRS, EDYTEM, 73000, Chambéry, France
[2]INSTAAR and Department of Geological Sciences, University of Colorado Boulder, Boulder, CO 80309, USA
[3]Université Grenoble Alpes, CNRS, IRD, IGE, Grenoble, France
[4]Université Grenoble Alpes, Univ. Savoie Mont Blanc, CNRS, IRD, IFSTTAR, ISTerre, 38000, Grenoble, France

Correspondence to: Benjamin Lehmann (lehmann.benj@gmail.com)

Abstract. Rock glaciers are some of the most frequent cryospheric landforms in mid-latitude high-elevation mountain ranges. Their activity strongly influences alpine environments over short (years to decades) and long (centuries to millennia) timescales. Being conspicuous expressions of mountain permafrost and important water reserves in the form of ground ice, rock glaciers are seen as increasingly important actors in the geomorphological and hydrological evolution of mountain systems, especially in the context of climate change. Over geological timescales, rock glaciers both reflect paleoclimate conditions and transport rock boulders produced by headwall erosion and therefore participate in shaping high mountain slopes. However, the dynamics of rock glaciers and their evolution over different timescales remain under-constrained.

In this study, we adopt a multi-method approach including field observations, remote sensing and geochronology, to investigate the rock glacier system of the Vallon de la Route (Combeynot massif, western French Alps). Remote sensing employing image correlation documents the displacement field of the rock glacier over modern timescales (1-10[1] years). Over longer periods (10[3]-10[4] years), we employ terrestrial cosmogenic nuclide ([10]Be in quartz) exposure dating on rock-boulder surfaces located along the central flow line of the rock glacier, targeting different longitudinal positions from the headwall to the rock-glacier terminus.

Our results show [10]Be surface-exposure ages ranging from 1.88 ±0.14 to 13.10 ±0.51 ka. The spatial distribution of rock-glacier boulders reveals a first-order inverse correlation between [10]Be surface-exposure age and elevation; and a positive correlation with horizontal distance to the headwall. These observations support the hypothesis of rock boulders falling from the headwall and remaining on the glacier surface as they are transported down valley, which thus can be used to estimate rock-glacier surface velocity over geological timescales. Our results also suggest that the rock glacier is characterized by two major episodes of activity. The first phase, starting around 12 ka, displays a [10]Be-age gradient that suggests a rock-glacier surface velocity of about 0.45 m/a. Following a quiescent period between ca. 6.2 ka and 3.4 ka, the present-day active upper two units have been emplaced during climatic conditions favoring rock-glacier motion at around 0.18 m/a. Those results allow us to quantify back erosion rates of the headwall between 1.0 and 2.5 mm/a, higher than catchment-integrated denudation rates

estimated over millennial timescales, suggesting that the rock-glacier system promotes the maintenance of high rock-wall
35   erosion.

1 Introduction and motivations

Rock glaciers are important geomorphic structures influencing the evolution of high-elevation mountain environments. Being lobated or tongue-shaped assemblages of poorly-sorted, angular rock debris and ice, rock glaciers move as a consequence of the deformation of internal ice, conveying large calibre sediments from high-elevation steep slopes, cirque headwalls to their
40   terminus at lower elevations (Barsch, 1977; Giardino and Vitek 1988). In the context of current climate change, rock glaciers are one of the most resilient cryospheric bodies in alpine environments (Jones et al., 2019). Indeed, they represent an important storage of water supply when pure-ice glaciers have disappeared (e.g., Williams et al., 2006; Jones et al. 2019). Over geological timescales, rock glaciers participate actively in the development of asymmetrical mountain crests by eroding and conveying rock from leeside headwalls (where rockfall is the primary source of debris) to lower elevations in the valley (Gilbert, 1904;
45   Johnson et al., 1980). Although rock glaciers have received considerable attention in the last couple decades, being catalogued in several geographic areas (see Jones et al. 2019 for latest review), how rock glaciers form and evolve is still a subject of debate, with two main holistic views (see Haeberli et al. 2006; Berthling, 2011). On one hand, rock glaciers are seen as periglacial features in which ice grows into debris interstices, forming an ice-rock mixture that creeps by the influence of gravity and sufficient slope (e.g., Wahrhaftig and Cox, 1959; Ikeda et al., 2008). On the other hand, rock glaciers are thought
50   to result from glacial remnants with a deforming ice core that are being protected by a continuous debris cover (e.g., Whalley, 1974; Anderson et al., 2018).

The development of rock glaciers is a long process taking few hundred to thousands of years (e.g., Berthling, 2011). Their morphology, activity and dynamics reflect present and past climates (i.e. temperature and precipitation fluctuations) and geomorphological forcing (rock and snow avalanching, bedrock structural patterns; Kellerer-Pirklbauer and Rieckh, 2016;
55   Jones et al. 2019). Rock-glacier activity is categorized between active, transitional and relict modes, and has been recently updated based on geomorphological indicators (RGIK, 2021). An active rock glacier presents movement in most of its surface, although a transitional rock glacier will present low movement only detectable by *in-situ*/remote-sensing measurement and/or restricted to areas of non-dominant extent. Finally, a relict rock glacier has no detectable movement and no morphological evidence of recent movement and/or ice content (RGIK, 2021). Rock glaciers have been documented to accelerate with
60   increasing temperature (Delaloye et al., 2010; Cremonese et al., 2011; Kellerer-Pirklbauer, 2017; Wirz et al., 2016; Eriksen et al., 2018; Kenner et al. 2018; Marcer et al. 2021) but when the ice content falls below a critical saturation threshold, rock glaciers stop creeping, turning from active into transitional and eventually relict mode (Sandeman and Ballantyne, 1996). Their activity is also controlled by the geomorphology of the surrounding topography. For instance, it has been suggested that when the rock-boulder delivery rate and debris/ice incorporation from the headwall becomes insufficient to sustain the insulation of

65 the ice-rich part, the activity of the rock glacier will decrease and stop regardless of the rock-glacier thermal state (Amschwand et al., 2021).

To better understand the relationships between external forcings and the activity of rock glaciers, and to assess how ongoing climate change has and will affect them, their past activity and in particular past vs. modern surface velocity estimates have to be quantified from annual to millennial timescales. Analytical advancements over the past decades have allowed significant

70 progress of the remote-sensing tools monitoring landscape changes in high-mountain regions (e.g., Necsoiu et al., 2016; Vivero and Lambiel, 2019; Blöthe et al., 2021; Robson et al., 2020). Indeed, methods such as LiDAR (Micheletti et al., 2017), InSAR (i.e., Liu et al., 2013; Barboux et al., 2014; Strozzi et al. 2020), aerial photogrammetry (i.e., Cusicanqui et al., 2021) and unmanned aerial vehicle systems (i.e., Dall'Asta et al. 2017; Vivero and Lambiel 2019) have remarkably improved the temporal and spatial resolution of surface velocity surveys for rock glaciers. A recent study (Cusicanqui et al., 2021) in the

75 western French Alps has shown the feasibility of using high-resolution digital elevation models (DEMs) and ortho-rectified images produced from combinations of historical aerial and satellite images to reconstruct the surface velocity of rock glaciers over the last seven decades. Extrapolations from short-term surface velocities have been used to estimate the rock-glacier formation time and to reconstruct their activity over longer timescales (e.g., Kaab et al., 1997; Bodin, 2013). However, it remains difficult to assess such extrapolations and to accurately constrain the long-term dynamics and morphological changes

80 of rock glaciers without reliable estimates over centennial to millennial timescales.

To improve our understanding of rock-glacier long-term dynamics and potential forcing mechanisms, relative and absolute dating methods have been applied on both active and relict rock glaciers (e.g. Haeberli, 2013; Amschwand et al. 2021). In rare cases, radiocarbon dating has been used on lacustrine sediments or trees buried by rock glaciers (Paasche et al., 2007) or on vegetal macrofossils found in the permafrost of rock glacier (Krainer et al., 2015). Schmidt-hammer dating has been employed

85 to date surface exposure for boulders from numerous rock glaciers (European Alps, Norway, Island and New Zealand) but such approach requires local calibration surfaces and often only provide relative dating (e.g., Böhlert et al., 2011; Scapozza et al., 2014; Matthews and Wilson, 2015; Winkler and Lambiel, 2018). Similarly, lichenometry has been applied successfully on rock glaciers with stable rock boulders at the surface, although absolute dating requires calibration of this technique (Konrad and Clark, 1998; Galanin et al., 2014). Optically stimulated luminescence has been used to quantify the travel time of buried

90 fine sediments in rock glaciers (Swiss Alps), but large uncertainties potentially coming from pre-burial bleaching of fine sediments make this approach challenging to apply at larger scale (Fuchs et al., 2013).

Terrestrial cosmogenic nuclide (TCN) dating has been successfully applied to constrain the exposure time of rock boulders at the surface of relict rock glaciers and their stabilization in the European Alps (Hippolyte et al., 2009; Steinemann et al., 2020), the Iberian Peninsula (Rodríguez-Rodríguez et al., 2017; Andrés et al., 2018; Palacios et al., 2020), Scotland (Sandeman &

95 Ballantyne, 1996) and Iceland (Fernández-Fernández et al. 2020), demonstrating their potential as independent paleoclimate archives to reconstruct past permafrost development and disappearance (Andrés et al., 2018). Cossart et al. (2010) combined [10]Be surface-exposure dating and weathering rind thickness to document three main generations of rock glaciers in the Southern French Alps. Recently, two studies (in Iceland and Switzerland) have applied TCN dating on rock glacier systems composed

of both active and relict units (Fernández-Fernández et al. 2020; Amschwand et al., 2021), showing deactivation and
100   stabilization of the rock glacier at lower elevations and further distance from the headwall.

The onset of rock-glacier development in the high-elevation parts of the European Alps is thought to have started after the onset of glacier retreat following the Last Glacial Maximum (around 19-18 ka in the European Alps, e.g., Wirsig et al., 2016 ; Monegato et al. 2017; Lehmann et al., 2020). Chronologies of rock-glacier development in the Alps of Austria, Central Switzerland and France have shown different rock-glacier generations: during the Lateglacial period (ca. 16 ka), during or
105   shortly after the Younger Dryas (ca. 12 ka) and during the Late Holocene, probably at the end of Subboreal period (5.2/5.0 - 4.3/4.2 ka) when the high-elevation cirques became ice-free (Cossart et al., 2010; Amschwand et al., 2021; Steinemann et al., 2020; Charton et al. 2021).

In this study, we present the reconstruction of activity and surface velocities at different timescales for the rock-glacier system of the Vallon de la Route (Combeynot massif, western French Alps). Remote-sensing methods such as image correlation over
110   photogrammetric products allow us to reconstruct the surface displacements field of the rock glacier over the last six decades. Over longer periods (10^3 to 10^4 years), we apply TCN dating (quartz ^{10}Be) to rock-boulder surfaces at different positions along the central flow line of the rock glacier, from the headwall to its terminus, allowing the conversion of the ^{10}Be surface-exposure ages into long-term surface displacement estimates. By discussing our estimates of rock-glacier surface kinematics at different timescales, we show that it is possible to reconstruct the past activity of the rock glacier and to use rock glaciers as independent
115   paleoclimate and paleo-geomorphological archives revealing the evolution of alpine environments.

2 Study site

The Combeynot massif (45°0N - 6°2E) represents the north-eastern part of the Ecrins Pelvoux massif, located in the western French Alps (Fig. 1a). The Ecrins Pelvoux massif presents high alpine topography, with summits above 4000 m a.s.l. and valley bottoms around 1000-1500 m a.s.l. Widespread U-shaped valley profiles, hanging valleys and glacial trimlines illustrate
120   the imprint of Quaternary glaciations on the massif (Delunel et al., 2010; Valla et al., 2010; Le Roy et al., 2017). Paleo-glacier reconstructions since the Last Glacial Maximum have been previously constrained using mapping, interpolation of glacial features and TCN dating applied on moraine deposits and glacially-polished bedrock surfaces (Delunel, 2010). Evidence for Younger Dryas stadial readvances have been mapped and dated in several catchments of the massif (e.g., Coûteaux and Edouard, 1987; Chenet et al., 2016; Charton et al., 2021). Based on surface-exposure dating of moraine deposits, few glacial
125   advances during the Holocene and more precisely during the Neoglacial (from ca. 4.3 ka) have been reconstructed (Le Roy et al., 2017 ; Shimmelpfennig et al., 2019, unpublished data ; Schoeneich et al., 2019, unpublished data). Modern glacierization is characterized by small cirque and slope ice bodies covering 68.6 km² in 2009 (Gardent et al., 2014). The two largest valley glaciers remaining today are the Girose Glacier (5.1 km²) and the Glacier Blanc (4.8 km²); most of the other glaciers are cirques or debris covered (Gardent et al., 2014; Fig. 1b in Le Roy et al., 2017).

130   Ranging from 1670 to 3155 m a.s.l., the Combeynot massif hosts 33 active and transitional rock-glacier systems and 38 relict rock glaciers (Bodin, 2013). These landforms range between 2000 and 2850 m a.s.l.; the root-zones mean elevation of the active rock glaciers is about 2700 m a.s.l., whereas the mean elevation of their frontal positions is 2620 m a.s.l. (Bodin, 2013). The Laurichard rock glacier, on the northern side of the Combeynot massif (Fig. 1a), is the site of one of the longest geodetic surveys for surface velocity in the European Alps (from the late 1970s; Francou and Reynaud, 1992; Thibert et al., 2018).

135   The Combeynot massif represents a slice of granitic intrusion confined in volcanic-sedimentary gneiss; a flysch layer of the ultra-Dauphinoise zone locally covers its eastern side (Barbier et al., 1973). The characteristic macro-crystalline scale fragility of the crystalline bedrock can be related to Pre-Hercynian hydrothermal activity. A network of NNW/SSE faults and a high density of diaclases cut the Combeynot massif, producing meter and sub-meter scale jointing of the bedrock (Francou and Reynaud, 1992). Thick superficial deposits (mostly coarse material) are the consequence of gravitational and nivo-periglacial

140   processes (cryoclastic and avalanche activity; Francou, 1982).

   From a present-day climatic point of view, the Combeynot massif is located in the transition zone between areas with a Mediterranean climate and areas with a more oceanic climate. Consequently, the local climatic setting is characterized by western frontal incursions and rainfall coming from the Italian side of the Alps and summer periods with low rainfall (Bodin, 2013). Regionally-available datasets (1971-2000) from weather stations located between 1324 and 2550 m a.s.l. suggest that

145   monthly air temperatures are negative over 4 months of the year at 2000 m a.s.l., and over 8 months of the year at 3000 m a.s.l. Also, for the 1961-1990 period, mean annual 0°C and –2°C isotherms were located at 2560 m a.s.l. and 2910 m a.s.l., respectively (Bodin, 2013).

   The Vallon de la Route catchment is occupied by neither debris-free nor debris-covered glacier but is sheltering a rock-glacier system of about 6.74×10^5 m^2. The total catchment area is about 4.41×10^6 m^2, is southwest facing and ranges from 1960 to

150   3155 m a.s.l. It is bounded upstream by the highest peaks of the massif, the Roc Noir de Combeynot (3112 m a.s.l.), the West Pic of Combeynot (3155 m a.s.l.) and the Tete de Pradieu (2879 m a.s.l.), and downstream by the torrent of the Rif de la Planche (Figs. 1a and 1b). The rock-glacier system is overhung by a debris source with area of about 5.351×10^5 m^2 (estimated horizontal projection of the surface) composed of leucogranitic bedrock (Fig. 1b). Geoelectrical measurements (2006) on the rock glacier have shown that the active layer reaches a maximum thickness of 9 m at 2630 m a.s.l. and that the ice-rich layer

155   does not exceed 15 m and may consist of ice-cemented debris, with occasional layers of higher ice contents (Bodin, 2013). The rock-glacier system of the Vallon de la Route (Fig. 1) was chosen because it presents the ideal attributes of a rock glacier for this study, namely (i) it has an active snout and sharp edges, (ii) its total length of order of 1 km long, (iii) its situation in the middle of a valley, and (iv) it has one single bedrock type in the headwall source (i.e., leucogranite).

3 Methods

3.1 Field observations and image correlation

3.1.1 Field observations

Geomorphological recognition was performed using the protocol described in the "Towards standard guidelines for inventorying rock glaciers, Baseline concepts" of the International Permafrost Association Action group for rock glacier inventories and kinematic (RGIK, 2020). *In-situ* visual inspection such as observation of the steepness of the front, description of ridge and furrow topography, size and shape distribution of the debris cover, together with DEM and landscape image analysis, were performed to geomorphologically classify the different landforms and their connection with each other. Five different units (I, II, III, IV and V) were identified from top to bottom according to *in-situ* geomorphological observations such as their elevation, their slope, their vegetation cover, the continuity and apparent activity of their landforms (elevation, average slope and covered area were determined using the 0.5-m LiDAR high resolution DEM; Figs. 1, 2, 3 and 4). Units are separated by either ridge and furrow topography or front, which are the expression of the gravity-driven buckle folding of rock glacier morphology (Frehner et al., 2015). In the present study, we focus our sampling strategy on 13 landforms (ridges) annotated from A to M (Table 1 and Fig. 5).

3.1.2 Orthomosaic production

The reconstruction of the rock-glacier surface displacement over decade timescales was done using the image correlation protocol developed by Cusicanqui et al. (2021). We compared timeseries of 4 different orthorectified images (1952, 1960, 1989 and 2018). The 3 oldest ones were generated using historical aerial photographs (1952, 1960, 1989 with 2 and 3 images, respectively) collected from the French National Institute of Geographic Information and Forestry (IGN, www.remonterletemps.ign.fr). Orthomosaics were computed with Agisoft Metashape (version 1.6) software using ground control points (GCPS, between 12 and 18 depending of the year) with coorinates collected from the IGN map service (www.geoportail.fr) and elevations using a high-resolution LiDAR DSM (0.5 m resolution) survey realized by SINTEGRA (2012).

For the latest period, the orthorectified image of 2018 was computed using stereo Pleaides high-resolution acquisition using Ames Stereo Pipeline (ASP) (Shean et al., 2016). ASP uses rational polynomial coefficients (RPCs) provided with the Pléaides images, eliminating the requirement of a large number of high accuracies GCPs. The DEMs and orthoimage were then co-registered using previous LiDAR high-resolution DEM and following Nuth and Kääb, (2011) methodology, the orthoimage was then shifted (translation-only) with co-registration values (x, y and z displacements). All original orthomosaics were resampled at a 0.5 m resolution and set in a common 3465 × 3541-pixel grid system.

3.1.2 Image correlation for surface displacement measurement

190   2D displacements of the rock glacier between orthomosaic pairs (1952, 1960, 1989 2018) were computed using the IMCORR module within the SAGA toolbox in QGIS (Scambos et al., 1992). The feature-tracking algorithm retrieves pixel patterns between two georeferenced images and attempts to match small subscenes (called 'chips') and produces shapefiles (points and lines) containing the 2D surface displacements. The program uses a fast Fourier transform-based version of a normalized cross-covariance method (Scambos et al., 1992). In the present study, several parameters of the algorithm were tested before settling

195   on the following: search chip size = 64 pixels; reference chip size = 32 pixels; grid space = 4 m for the pair 1952-1960; 1960-1989 and 1989-2018. The 2D displacement of the 1960-2018 pair, giving the most accurate results regarding the largest time difference, was calculated using the following parameters: search chip size = 128 pixels; reference chip size = 64 pixels; grid space = 10 m.

The obtained surface displacements were manually filtered according to (a) different local spatial coverage and artifacts (e.g.,

200   related to random local similarity of the coarse blocky surface; Bodin et al. 2018), (b) lack of consistency of the displacement between neighboring vectors (difference >30°), and (c) outlier displacement values (Cusicanqui et al., 2021). Finally, 5.4% of the points were removed for the pair 1960-2018. The ±1σ variability is calculated using all the pixels for each unit together with the median displacement. The displacements obtained on the rock-glacier system are compared to the measured displacements of a control area selected to be within stable terrain of about 1.25×10^4 m^2 below the lower part of the rock

205   glacier, where no displacement should be observed (dashed outlined area in Fig. 2). This control area has been chosen to be outside of the rock-glacier system, out of the scree field and with local slopes <30°. The absence of movement (solifluction, creeping, landsliding) has been determined by inspecting historical aerial photographs collected from the IGN-France.

3.2 ^{10}Be surface-exposure dating

3.2.1 Sampling

210   We collected 19 rock-boulder samples with approximately 0.5 kg of rock material from the 13 landforms of interest (Tables 1 and 2; Fig. 3). For 6 of these landforms (B, C, E, G, J and M, Table 1) two different boulders were sampled in order to evaluate the reproducibility of our dating approach (Fig. 2c). The boulders were chosen following the central flow line which was defined to be both at the centre of the rock glacier width and perpendicular to the main ridge and furrow topography landforms (black line in Fig. 3 and Fig. 5), from the high-elevation active lobes to the terminus of the rock glacier system. Sampled

215   boulders were chosen on the top of the ridges to minimize topographic shielding, snow-cover effect and complex exposure histoires (covering of sediment and clasts, late exhumation; Fig. 2c). Suitable boulders are large (>1.5 m) and in a stable position (Figs. 2c and 2d). Appropriate rock surfaces do not show sign of intense weathering or recent chipping. Sampling was done using a hammer, a chisel and a small electric circular saw during 4 days (28/09/20-01/10/20). The sampling details of each rock boulder are summarized in Tables 1 and 2.

3.2.2 TCN preparation and [10]Be measurement

Samples were crushed and sieved to retain the 200-500-µm grainsize fraction. Beryllium extraction was performed at the GTC platform (ISTerre, France) using a chemical protocol adapted from Brown et al. (1991) and Merchel and Herpers (1999). Magnetic separation was used to isolate the quartz fraction, followed by successive leaching in an H_2SiF_6/HCl mixture. In order to speed up the purification of quartz and save leaching cycles, magnetic separation with fine magnetite powder was performed between leaching cycles, to remove partially altered minerals. Meteoric Be purification was achieved with three sequential dissolutions using diluted HF (Kohl and Nishiizumi, 1992). The purified quartz samples (13-26 g for each individual sample) were completely dissolved in concentrated HF after being spiked with ~510 mg of a 998 mg/L Be carrier solution (Scharlab ICP Standard, batch 16107901) in order to fix the [10]Be/[9]Be ratio (Table 2). After HF evaporation, perchloric and nitric acids were added and evaporated to remove organic compounds and fluorides. Beryllium was extracted by successive alkaline precipitations of $Be(OH)_2$ alternated with separation on anion and cation columns. Samples were then oxidized at 700°C for 1h and the final BeO mixed with Nb powder and loaded into nickel cathodes. [10]Be concentration were measured at ASTER national facility (Cerege, France) against standard BeO_STD-11 ($1.191 \pm 0.013 \times 10^{11}$; Braucher et al., 2013) and were corrected for the full process blank with a [10]Be/[9]Be ratio of $6.278 \pm 0.534 \times 10^{-15}$.

3.2.3. Surface-exposure age calculation

Surface-exposure ages were computed with the CREp online calculator (Martin et al., 2017) using the LSD scaling scheme (Lifton et al., 2014), the ERA40 atmospheric model (Uppala et al., 2005) and the Lifton VDM 2016 geomagnetic database (Pavón-Carrasco et al., 2014). We used the Chironico landslide production rate (with sea-level high-latitude value of 4.16 ± 0.10 atoms.g/qtz/a; Claude et al., 2014), scaled according to the sample longitude, latitude and elevation.

The production rate was corrected for sample thickness (Table 2) and density (2.75 g cm^{-3}). Shielding correction includes the topographic shielding due to surrounding landscape and the dip of the sampled surface calculated with the online calculators CRONUS-Earth (Balco et al., 2008, http://hess.ess.washington.edu/math). In addition, we explore the influence of snow-cover attenuation using the Gosse and Phillips (2001) equation with snow density of 0.3 g/cm^3 and an attenuation length for fast neutrons in snow of 150 g/cm^2 (Delunel et al., 2014). According to a previous study dating a rock avalanche less than 1 km north of our site (Chenet et al., 2016), we use an estimate of 50 cm cover of snow for 6 months of the year, values that are most often cited in the literature for the Alpine regions for these altitudes areas (Hormes et al., 2008; Ivy-Ochs et al., 2006; Kelly et al., 2004; Schindelwig et al., 2012; Wirsig et al., 2016; Chenet et al., 2016). We do not consider the effects of boulder surface erosion, consequently reported [10]Be surface-exposure ages must be seen as minimum estimates but according to the age range they can be considered as the time duration of boulders on the rock glacier.

4 Results

4.1 Field observations

Unit I (ranging from 2867 and 2685 m a.s.l.) and unit II (ranging from 2735 and 2626 m a.s.l.) were classified as active and cover areas of about 7.29 and 5.42 $\times 10^5$ m^2, respectively. They present evidence of downslope creep movement such as steep fronts (steeper than the angle of repose), strongly marked ridges-and-furrows topography, absence of vegetation cover and active layers composed of decimetric to metric angular debris. These two units are talus-connected, meaning that they are part of a downslope sequence including headwall – talus slope – rock glacier (Figs. 2a-b). The delivery of debris is likely accomplished by rockfall activity, surface runoff, debris flow and/or avalanche events from the headwall bedrock. The horizontal limit between the talus slope and rock-glacier units is determined with about 50 m of uncertainty. Unit III, spanning from 2685 to 2556 m a.s.l. and covering 1.550 $\times 10^5$ m^2, was evaluated to be transitional. Indeed, the evidence of downslope movement is less visible (but still detectable) than for units I and II, the ridge-and-furrow topography is less prominent. Finally, units IV and V, with elevation ranges of 2718-2557 and 2585-2521 m a.s.l., respectively (and covering about 1.776 $\times 10^5$ and 2.147 $\times 10^5$ m^2, respectively), clearly display relict morphologies with no geomorphological evidence of recent surface movement. Their metric to pluri-metric debris layers are highly covered by superficial material and vegetation. This top to bottom organization from active, to transitional and relict units is common in alpine settings.

4.2 Image correlation

As described in section 3.2, we used pairs of orthorectified images to reconstruct surface displacement of the rock-glacier system. After testing all the possible combinations between the four orthorectified images (1952, 1960, 1989 and 2018), the 1960-2018 pair was chosen for being the most adapted to reconstruct the activity of the rock-glacier system over decadal timescales. As the aim of this study is to compare modern to Holocene rock-glacier activity, we focus on the integrated displacement over the longest and best-quality time series (1960-2018) instead of focusing on shorter-scale variations in surface displacement over modern timescales (e.g., Cusicanqui et al., 2021). The 1960-2018 correlation gives the most extended spatial coverage and lead to the best image correlation results with respect to the difference in shading, snow cover and quality between the two rectified images. The results of the time series 1952-1960, 1960-1989 and 1989-2018 can be found in the supplementary material (Fig. A2).

Figures 3 and 4 present the results obtained using the IMCORR feature-tracking module. The control area (dashed outlined area in Fig. 3) within stable terrain shows an averaged displacement of 1.55 ±0.92 m, which we use as a threshold value to control the confidence level of our image-correlation protocol. This threshold value corresponds to failed correlation in between pixel group and does not correspond to real surface displacement. Consequently, all rock-glacier areas showing surface displacement lower than 1.55 m should be considered stable (dashed area in Figs. 4a-b).

Surface displacements calculated over the entire rock-glacier system for the last 58 years (i.e., between 1960 and 2018) show a maximum value of 16.9 m, with a median displacement of 1.7 m and a standard deviation of 4.2 m over the total rock-glacier

area. The spatial distribution (Fig. 3) and the longitudinal transect (Fig. 4a, location by red line in Fig. 3) show that significant surface displacements are concentrated in the upper part of the rock-glacier system. Indeed, units I and II show median surface displacements over the 1960-2018 period of 8.1 ±4.7 m and 8.4 ±3.0 m, respectively (values calculated for all the values inside

285 each unit, Table 5). This agrees with our classification as "active" from geomorphological observations (Fig. 2 and Section 4.1). Unit III presents surface displacements of 2.0 ±1.5 m, which is just above the detection limit. Our classification of transitional activity (Section 4.1) thus seems appropriate. Finally, units IV and V, with median displacement of 1.0 ±0.6 and 1.2 ±0.4 m, respectively, are below the detection limit (Table 5, Figs. 3 and 4b). These parts of the rock-glacier system can thus be considered without modern motion, and correspond well with the relict classification determined from

290 geomorphological observations (Section 4.1). The rock glacier becomes inactive around 945 m from the headwall, corresponding to an elevation of about 2600 m a.s.l. Also, two displacement peaks can be observed in the upper part of the rock glacier system (Figs. 3 and 4a), one in unit I and another in unit II, potentially indicating different debris sources for the two units.

4.3 Surface-exposure dating results

295 Figures 5 and 6, together with Tables 2-4, present the analytical results of ^{10}Be surface-exposure dating for each individual boulder sample, as well as for statistics within landforms and units. Our ^{10}Be-age results range from 1.88 ±0.14 to 13.10 ±0.51 ka for the entire dataset. The correction for snow-cover shielding ranges between 7 and 9% between samples. In view of the controversy over whether wind could remove snow from moraine/rock-glacier ridges during the Holocene period (Federici et al., 2008; Schimmelpfennig et al., 2014; Moran et al., 2016; Chenet et al. 2016), we refrain from correcting the output ^{10}Be

300 ages for snow cover in the following discussion. This imply that the obtained ^{10}Be ages, with neither snow-cover nor surface-erosion correction, are considered as minimum estimates.

Our results clearly reveal a first-order inverse correlation between ^{10}Be surface-exposure age and elevation, and a positive correlation between ^{10}Be surface-exposure age and horizontal distance from the headwall (Fig. 6). These correlations support the hypothesis that rock boulders originate from the headwall and are then transported downward on the surface of the rock

305 glacier: the further from the headwall (and the lower the elevation) the boulder is, the older its ^{10}Be surface-exposure age. These correlations remain valid when we consider the weighted-average ^{10}Be surface-exposure ages for every landform (Figs. 6c-d, Table 3) and unit (Figs. 6e-f, Table 4).

If considered in more detail, the ^{10}Be-age dataset shows two clusters: cluster 1 combining the highest units I and II, and cluster 2 including the lowermost units (III, IV and V). Cluster 1 shows ^{10}Be ages between 1.88 ±0.14 and 4.88 ±0.29 ka; and cluster

310 2 presents ^{10}Be ages between 9.25 ±0.40 and 13.1 ±0.51 ka. These results agree with the geomorphological classification we proposed for these rock-glacier units: units I and II as active, unit III as transitional, and units IV and V as relict.

5 Discussion

5.1 Inheritance/pre-exposure and loss/incomplete exposure

315 The measured [10]Be concentrations of rock-glacier boulders surfaces should always be interpreted with caution as multiple external processes can affect it. Surface erosion can cause a depletion of [10]Be concentration at the rock-boulder surface, as well as complex exposure histories (discontinuous exposure, snow/sediment covering), both of which would lead to an underestimation of the "accurate" [10]Be surface-exposure age (7% and 9% in the specific case for snow cover, see Section 4.3). On the other hand, inheritance (i.e., headwall pre-exposure before rock collapse on the rock glacier), will lead to overestimation

320 of the [10]Be surface-exposure age.

We employ linear regression of the [10]Be dataset presented in (Fig. 6) to evaluate the source of debris elevation and estimate the inheritance/pre-exposure of investigated boulders (Amschwand et al., 2020). For instance, when we calculate the intercept of cluster 1 regression (i.e. elevation at which the [10]Be surface-exposure age is null), we obtain an elevation of 2737 m a.s.l.; whereas if we include all the samples together (red and black dotted lines in Fig. 6a, respectively), we obtain 2748 m a.s.l.

325 From our geomorphological observations, the elevation at which the talus slope connects to the headwall is close to 2880 m a.s.l. (mean elevation of the foot of upper headwall), which may safely be considered the elevation at which debris are delivered to the rock glacier. The difference between the different elevations mentioned above could lead to the interpretation that the [10]Be surface-exposure ages are underestimated. This can be explained by the fact that our sampling strategy was targeting the biggest boulder at the surface of the rock glacier, so that the likelihood of any burial event was minimized. The metric and

330 pluri-metric boulders we sampled might roll far from the cliff and might therefore be incorporated onto the rock glacier surface at a higher distance/lower elevation than the present-day limit between the talus and the headwall. The relationship between [10]Be surface-exposure age and elevation is also dependent on the relation between elevation and distance along the rock glacier (i.e., hypsometric distribution of the rock-glacier surface) and the potential inheritance/pre-exposure effects on the measured [10]Be concentrations.

335 Linear regression between horizontal distance from the headwall and [10]Be surface-exposure age allows us to quantify potential inheritance/pre-exposure bias (Fig. 6b). By considering cluster 1, the samples have experienced inheritance/pre-exposure of about 2.16 ka (intercept of red dashed line in Fig. 6b). This assumes that (i) blocks fall at the talus/headwall contact and, (ii) the displacement rate is continuous over the temporal range of the considered [10]Be surface-exposure ages. Once again, this inheritance/pre-exposure estimate has to be put in proper geomorphic perspective, as units I and II do not share the same

340 headwall source (with potentially different slope aspects and thus different erosion rates), unit II being more to the southeast (Section 4.2). When regressed individually for units I and II, potential inheritances are about 1.59 and 2.79 ka for units I and II, respectively. For above calculations, we only used samples from cluster 1, being the youngest and closest to the headwall. Samples from cluster 2, with the oldest [10]Be surface-exposure ages and the greatest distances from the headwall, could also involve other biases that include non-continuous displacement rate over this timescale and loss/incomplete exposure due to

345 surface erosion or tilting and burial of the sampled surface.

To assess the reproducibility of our dating approach, we sampled 2 different boulders on 6 of the rock-glacier ridges (landforms B, C, E, G, J and M; Figs. 2d, 5 and 7). The minimum and maximum horizontal distances between two replicates are about 8 and 82 m for landforms J (samples VR12 and VR13) and B (samples VR12 and VR13), respectively; a minimum elevation difference of about 2 m for landforms G (VR8 and VR9) and M (VR16 and VR17) and a maximum elevation difference of 14

350 m for landform (J) (Fig. 5 and Tables 1 and 2). Significant variability in ^{10}Be surface-exposure age occurs at the landform/ridge scale, although it does not affect the output correlations discussed above (Table 3 and Fig. 6). Landform C presents the higher age variability (99%, ^{10}Be surface-exposure ages of 1.32 ±0.21 and 4.88 ±0.29 ka for samples VR2 and VR3, respectively, Table 3 and Fig. 7). The age variability of the other landforms is correlated with the elevation and anticorrelated with the distance to the headwall (26%, 13%, 10%, 8% and 2% of age variability for 2 samples per landform for landforms B, E, G, J

355 and M, respectively, Table 3 and Fig. 7). Only landform M displays variability that is smaller than the absolute uncertainty on individual ^{10}Be surface-exposure ages, and may therefore be considered non-significant. The same pattern is observable for variability at the scale of the units (Table 4 and Fig. A3). Samples from cluster 1 show much higher variability than samples from cluster 2. A first interpretation is that samples that the variability is smoothed between samples during transport an exposure on the rock glacier (cluster 2). We interpret this as highlighting that the events of tilting, burial and/or erosion of the

360 sampled boulders do not strongly influence the reported ^{10}Be surface-exposure ages, and that the variability likely arises instead from differing exposure times on the headwall prior to rockfall delivery onto the rock-glacier surface. Secondly, the importance of inheritance/pre-exposure events would have less importance for the oldest ^{10}Be surface-exposure ages than for the youngest ^{10}Be surface-exposure ages. The high variability in cluster 1 ^{10}Be surface-exposure ages could be explained by variation in ^{10}Be inheritance due to pre-exposure in the headwall. Using the difference in ^{10}Be concentration between replicates, we

365 estimated an inheritance considering that the ^{10}Be concentration difference for each replicate correspond to a ^{10}Be production rate at the elevation of rock in the headwall (taken as 2997 m a.s.l. middle elevation of the cliff source). Results show age differences of about 0.88 ±0.04, 2.88 ±0.47, 0.39 ±0.03, 1.06 ±0.04, 0.67 ±0.03, 0.17 ±0.01 ka for landforms B, C, E, G, J and M, respectively (Table 3). The median value of those results is 0.78 ±0.97 ka and can now be compared to the inheritance estimate of 2.16 ka using linear regression between ^{10}Be surface-exposure age and distance to the headwall of cluster 1.

370 We interpret the observed variability in ^{10}Be surface-exposure ages as representing the stochastic nature of rockfall events. This leads to both different residence times of boulders in the headwall before rock fall, and different sites of incorporation of boulders in the talus/rock glacier system. Interestingly, all sample ^{10}Be surface-exposure ages suggest low inheritance compared to other settings in the European Alps. In the Mont Blanc massif, for example, the more competent granitic spurs result in potential inheritance of >10 ka (Gallach et al. 2018; 2020) with commensurately lower rate of debris supply and

375 lower frequency of rockfall events (see Section 5.3 for discussion about headwall erosion rates).

5.2 Surface velocity comparison and reconstruction

Figure 8 and Table 5 compile and illustrate the rock-glacier surface velocities calculated from the ^{10}Be surface-exposure dating and from the correlation of aerial and satellite orthorectified orthomosaics. When considering ^{10}Be surface-exposure dating,

the mean surface speeds were calculated by dividing the distance to the headwall of either the individual sample or the unit

380   (mean distance to the headwall evaluated at all pixels inside within the unit limits) by their corresponding individual or median [10]Be surface-exposure ages. Here we assumed that the [10]Be surface-exposure age represents exposure between the time of the rockfall event that delivered the block to the surface of the headwall/talus transition and its arrival at the sample site. The modern velocities from remote sensing analysis are calculated by dividing the measured displacement or the median values for each unit, by the time between the two orthorectified images, in this case 58 years (1960-2018).

385   The surface velocities based upon [10]Be surface-exposure dating range from 8.3 ±0.4 to 33.3 ±5.3 cm/a with a median value of 13.1 cm/a and a standard deviation of 6.4 cm/a (Fig. 6). When we average over the different units, the calculated surface velocities range from 8.9 ±1.1 to 17.9 ±11.3 cm/a (Table 5). While no correlation between the distance from the headwall and the surface velocity is clearly visible; the variability in surface velocity is significantly higher for units I and II. The difference between units I and II likely reflects their different debris- and snow-avalanche sources; they may therefore have independent

390   age and speed profiles. As a consequence, this could lead to an overestimation of the distance to the headwall for unit II (as the central line is defined with respect to Unit I, Fig. 5), and by consequence to an overestimation of its surface velocity.

For the remote-sensing analysis, we define a detection limit of 2.7 cm/a corresponding to the median speed of the control area (Figs. 3 and 4). As the displacements of units IV and V show surface velocities below the detection limit, we consider them immobile over the six last decades. Measurable motion occurs above 2600 m a.s.l., with velocities of 3.4 ±2.6 cm/a in unit III.

395   The upper units display higher velocities of the same order, about 13.9 ±8.0 and 14.6 ±5.1 cm/a for units I and II, respectively. Once more, these observations validate our proposed geomorphological classification for the activity of the different units (units I and II: active, unit III: transitional and units IV and V: relict).

One striking observation is that active units (I and II) share similar surface velocities but these are also comparable between long-term and short-term approaches (blue and red dataset on Fig. 8). Integration of the short-term surface velocities over the

400   late Holocene appears to predict well the [10]Be surface-exposure ages of investigated rock-glacier boulders. This suggests that the climatic and geomorphological conditions controlling the activity of the rock glacier have been stable above 2600 m a.s.l. over the last ca. 5 ka.

5.3 Rock glacier activity

In the following, we propose a possible history for the rock-glacier activity that includes two pulses of constant surface velocity.

405   Figure 9 presents schematically our interpretation of the repartition of the two clusters of [10]Be surface-exposure ages according to their distances from the headwall (Figs. 6b and 10b). During a first phase of activity, boulders fall from the headwall onto the surface of the rock glacier (Fig. 9a). The random distance from the headwall at which the boulder is incorporated in the rock glacier is representing the stochasticity of rockfall travel. The [10]Be inheritance corresponding to the residence time of the rock in the headwall is also stochastic. As rockfall-derived boulders are transported down-valley, both their [10]Be surface-

410   exposure ages and distances from headwall increase from these initial values (red lines in Fig. 9a). When the motion halts (presumably because the rock glacier thins beyond some threshold thickness), this first phase of activity ends, and boulders

remain stationary while their ^{10}Be surface-exposure ages continue to increase (Fig. 9b). Finally, a new phase of activity begins at the base of the talus (red points in Fig. 9c), and the new rock glacier overrides the up-valley boulders on relict forms (shadow points in Fig. 9c). In this conceptual model, we assume that the first phase of activity transports the boulders further

415 downstream than the second phase of activity.

We therefore argue that cluster 2, corresponding to ^{10}Be surface-exposure ages of units III, IV and V, represents a first phase of activity of the rock glacier, and that cluster 1, with units I and II, represents a second phase of activity. To constrain both the timing and the surface velocities of these phases of activity, we numerically simulate the evolution of ^{10}Be surface-exposure ages of boulders during their movement at the surface of the rock glacier (Fig. 10b). To represent its stochasticity, we prescribed

420 the inheritance (b in Fig. 9) with random values between 0 and 2.16 ka (as determined in Section 5.1). In the same way, the distance of incorporation of boulders on the rock glacier surface (a in Fig. 9) is randomly sampled between 0 and a maximum of 100 m. In this model, 3 different times should be prescribed. The initiation of the first phase of activity is set at 12.1 ka (t1 in Fig. 10a), which is the ^{10}Be surface-exposure median age of unit V. The second phase of activity is set to start at 3.4 ka (t3 in Fig. 10a) as this is the ^{10}Be surface-exposure median age of unit III and is still active now. Only the time at which the first

425 phase of activity ends cannot be directly extracted from the experimental data (t2 in Fig. 10a). Consequently, we simulate the ^{10}Be surface-exposure age structure of the rock-glacier complex for 100 values of t2 ranging from t3 (3.4 ka) to the youngest age of cluster 2 (i.e., 9.25 ka for sample VR8). The velocity of phase 1 is calculated using the maximum distance a block travelled at the surface of the rock glacier (1720 m) and the activity duration of phase 1 (t1-t2). The velocity of phase 2 is fixed at 0.22 m/a, value calculated using the maximum distance a block travelled at the surface of the rock glacier during this phase

430 (740 m) and the time of activity (t3 in Fig. 10a).

The 100 simulations are evaluated against the measured ^{10}Be concentrations using chi-square per degree of freedom, $\chi^2_v = \frac{\chi^2}{v}$.

The chi-squared is a weighted sum of squared deviations: $\chi^2 = \sum_i \frac{(O_i - C_i)^2}{\sigma_i^2}$ where σ is the variance on our ^{10}Be dataset, O are the observations, and C are the modeled data. The degree of freedom, $v = n - m$, equals the number of observations n minus the number of fitted parameters m (here 4: maximum inheritance, maximum distance of incorporation of a boulder on the rock

435 glacier, initiation of phase 1: t1 and phase 2: t3). The likelihood probability function is then calculated as $\mathcal{L} = 1/\exp\left(\chi^2_v / 2\right)$ and normalized with its maximum in order to extract the median value and the standard variation ($\pm 1\sigma$) of t2 (Fig. 10c). The inversion results show that the first phase of activity lasted from 12.1 to 6.26 $\pm$1.96 ($\pm 1\sigma$) ka, with a surface velocity of 0.29 $\pm$0.15 ($\pm 1\sigma$) m/a. The second phase of activity starts at 3.4 ka and has a surface velocity of 0.22 m/a (Fig. 10a). The more recent phase of activity overrides the ^{10}Be surface-exposure ages of the two upper units. We now discuss how these two phases

440 of rock-glacier activity can be connected to what is known about the paleo-environmental conditions in the western European Alps.

5.4 Reconstruction of paleo-environmental conditions

In the European Alps, the final Lateglacial period (i.e., Younger Dryas) led to readvance of the mountain glaciers reaching a
445   maximum extent around 12 ka for both the eastern and western Alps (e.g., Ivy-Ochs et al., 2008; Protin et al., 2019). Directly downstream of the Vallon de la Route catchment, [10]Be surface-exposure ages of moraines show ages of 13.0 ±1.1 ka and 12.4 ±1.5 ka, providing evidence for two stages of glacial advance or standstill at the end of the Lateglacial period (Chenet et al., 2016). Immediately after the onset of the Alpine glacier retreat (12.2 ±1.5 ka in the same valley, Chenet et al., 2016), several advance episodes lasting ~1 ka were identified (in the Ecrins massif), before the retreat starts again at ~10.4 ka (in the Mont
450   Blanc massif, Protin et al., 2019). Cossart et al. (2010) reported histories of glacier retreat and rock-glacier generation in the Clarée valley (about 10 km to the east of our study site). They identified three generations of rock-glacier development during the second half of the Holocene, ranging in elevation from ~2400 to 2800 m a.s.l.

In the Vallon de la Route catchment, the first phase of rock-glacier activity appears to start around 12.1 ka from our oldest [10]Be surface exposure age (Unit V). We suggest that this coincides with the final glacier retreat at the end of the
455   Lateglacial period. The upper mountain catchments and cirques then became free of glacier, allowing the headwall and scree field to feed a rock glacier with debris thickness sufficient to insulate the ice. In this case, the rock-glacier development would be considered to be geomorphically-controlled by contrast to a climatic control (Cossart et al., 2010). According to our reconstruction, the second generation of rock-glacier development occurred at about 3.4 ka. This is earlier than the estimate proposed by Bodin (2013) from the relationship between slope and velocity, with an estimated time of 1.7 ka for debris to
460   reach the front of unit I lying at around 2740 m a.s.l.

Whereas lateral glacier moraines dated using [10]Be surface-exposure approach suggest minor but several glacier re-advances between ca. 4.25 and 0.92 ka in the main glacierized valleys of the Ecrins-Pelvoux massif (Le Roy et al., 2017), there is no evidence for glacial re-occupation during the Neoglacial/Little Ice Age periods in the Vallon de la Route. This specific cirque does not share upstream connection with any of the main glacierized valleys of the massif. The headwall and scree
465   taluses were ice free and could therefore feed the rock-glacier system with debris and snow avalanches, maintaining the rock glacier during the last 3.4 ka, while the Neoglacial/Little Ice Age climate was favourable for glacier/rock glacier activity. Recent dating of Charton et al. (2021) on two rock glaciers located ~3 km to the north of our site and at an elevation of about 2050 m a.s.l. reveals [10]Be surface-exposure ages of ca. 11 ka. In their study, Charton et al. (2021) interpreted the [10]Be surface-exposure ages as marking the end of activity of the rock glacier. In the present study, we interpret the [10]Be surface-exposure
470   ages of the relict units as being the sum of its residence time on the headwall cliff, the time spent traveling on the surface of the rock glacier, and the time since deactivation of the relict portion of the rock glacier. Consequently, the inspection of the age structure of our rock glacier agrees with the following interpretation. The age structure (Fig. 10b) suggests two episodes of motion (Fig. 10a). The first phase, starting around 12 ka, displays a gradient in age with rock-glacier surface velocity of about 0.45 m/a. The rock-glacier activity then declines and stops at 6.26 ±1.96 ka. By around 3.4 ka, the climate again becomes
475   conducive to rock glacier motion at elevations above 2600 m a.s.l. and the presently active upper two units are emplaced.

Again, the [10]Be surface-exposure ages reveal an age gradient that reflects the surface velocity of 0.18 m/a (Fig. 10a) which agrees with modern estimates.

5.5 Headwall erosion and implications

480   The reconstruction of the rock-glacier activity provides a way to quantify the erosion rate of the surrounding headwalls over Holocene timescales. Bodin (2013) has performed geophysical measurement of the rock-glacier area and could determine a maximum thickness of the active layer of about 9 m and a maximum thickness of the ice-rich layer of about 15 m at 2630 m a.s.l. The entire area of the rock glacier is 6.745×10^5 m^2. An approximation of the total volume of debris, considering a total thickness of between 9.5 m (active layer thickness of 5 m and ice-rich layer of 4.5 m thick at 2720 m a.s.l.; Bodin, 2013) and

485   24 m (combining maximum of active layer thickness of 9 m and ice-rich layer of 15 m thick at 2630 m a.s.l.; Bodin, 2013), gives respectively 3.37×10^6 and 13.49×10^6 m^3. Regarding the low surface velocity estimated between 1968 and 2018, between 0.14 and 0.03 m/a over 42% of the total area (units I, II and III) and no movement of the other 58% of the total rock-glacier area (units IV and V), we can assume a negligible ice concentration over the all volume of the rock-glacier system. We then integrate this volume of debris over 12.1 ka (the median [10]Be surface-exposure age of unit V), we consider that all boulders

490   are derived from bedrock exposed above the rock glacier system (about 5.351×10^5 m^2), and can thus calculate a mean rate of erosion of the headwalls of between 1.0 and 2.5 mm/a. These results agree with estimates of erosion rate (~1.2-4.1 mm/a) from the granodioritic headwall of Bleis Marscha rock glacier in the eastern part of the Swiss Alps (Amschwand et al., 2021). The catchment-wide denudation rate of the Ecrins-Pelvoux massif has been estimated to range from around 0.3 to 1.1 mm/a on millennial timescales using [10]Be concentrations in stream sediment (Delunel et al., 2010), suggesting that frost-cracking

495   processes strongly control the post-glacial topographic evolution of mid-latitude mountain belts. The high erosion rates estimated in our study highlight that the steep rock walls that serve as the sources for debris on the rock glacier are retreating rapidly. This may be aided by the downstream conveyance of boulders/debris by the rock glaciers that prevent the headwalls from burying themselves in their own debris. This system therefore promotes the maintenance of high rockwall erosion rates and the development of cirques.

500   **Conclusion**

In this study, we quantitatively constrain the surface displacement field of an alpine rock-glacier system over Holocene and modern timescales by using both remote-sensing and geochronological datasets. The [10]Be surface-exposure dating of individual boulders sampled following the main center line of the rock glacier reveal ages from 1.8 to 13.1 ka, corresponding to elevations of 2751 and 2535 and m a.s.l., respectively. Our first-order observation shows an inverse correlation between

505   [10]Be surface-exposure age and elevation as well as a positive correlation between [10]Be surface-exposure age and distance from the headwall. This confirms the simple conceptual model in which rock debris falls from the headwall and remains on the surface as they are transported down valley by the rock glacier. Comparison of replicates from the transverse ridges along the

rock glacier show that loss/incomplete exposure due to surface erosion, burial or tilting of the boulders is negligible. These replicates also show that [10]Be concentrations of boulders close to the headwall can vary, constraining any inheritance/pre-

510 exposure effect. We estimate the possible maximum inheritance of 2.16 ka in our studied area, corresponding to the residence time of boulders in headwall.

The inverstigation of orthoimages from both aerial (1960) and satellite (2018) surveys shows that the rock-glacier system is composed of two uppermost active units with surface velocity of about 0.14 m/a at elevations from 2867 and 2626 m a.s.l., and a transitional unit with surface velocity of about 0.03 m/a at elevations between 2685 and 2556 m a.s.l. Analysis of a stable

515 area outboard of the rock-glacier system constrains the detection limit to be 0.02 m/a. Reported values of less than this detection threshold implies that the downstream part of the rock glacier below 2600 m a.s.l. is immobile, confirming our geomorphic analysis or the feature as relict. The comparison of the surface velocity estimated using the [10]Be surface-exposure dating relative to distance to the headwall, and from the surface displacement integrated over the 1960-2018 period between the orthoimage surveys, shows that late Holocene and modern velocities are comparable on the active units of the rock-glacier

520 system.

Our results suggest an activity of the Vallon de la Route rock glacier consisting of two main phases of surface displacement. The first episode lasted between about 12.1 ka and 6.26 ±1.96 ka, with onset around the end of the Younger Dryas cooling event, when the cirques became ice free, allowing the headwall and scree field to feed the rock glacier with debris, with insulation of the ice beneath. After a period of quiescence, the second phase of activity started around 3.4 ka and continues to

525 the present, possibly attributed to the favourable climate of the Neoglacial/Little Ice Age periods. Finally, we use the surface velocity obtained using [10]Be surface-exposure dating to reconstruct the erosion rate of the headwalls. The output erosion rates are between 1.0 and 2.5 mm/a. These are higher than catchment-wide denudation rates estimated over millennial timescales over the entire Ecrins-Pelvoux massif, suggesting that the rock-glacier system promotes the maintenance of high rock-wall erosion (back-wearing) rates and the development of cirques. To go further in reconstructing the paleo-environmental

530 conditions of this specific region, physically-based numerical modeling of rock glacier evolution (e.g., Anderson et al., 2018) should be applied using the existing topography, the spatial patterns of [10]Be surface-exposure ages and the modern surface velocity as modeling targets.

Author contribution

535 BL and RSA designed the study. BL and XB chose the study site and collected the samples in the field. PGV and JC supervised the TCN lab work of BL and provides the financial support for the TCN dating. BL and DC performed the remote-sensing analysis. BL and RSA wrote the numerical modelling experiments. All authors contributed to the writing of the manuscript.

Competing interest

540 The authors declare that they have no conflict of interest.

Acknowledgements

This study has been funded through the Mobility followship P2LAP2_191400 of the Swiss National Science Foundation. The authors acknowledge the Joseph Fourier alpine station for providing logistical and hosting support during the field campaign and the ASTER team (K. Keddadouche, G. Aumaitre, R. Braucher and V. Godard) for AMS analyses. The TRB team (ISTerre) is acknowledged for providing financial support for TCN dating. P.G.V. acknowledges funding from the Swiss National Science Foundation SNSF (Grant 639 PP00P2_170559) and the French ANR-PIA programme (ANR-18- MPGA-0006).

References

Amschwand, D., Ivy-Ochs, S., Frehner, M., Steinemann, O., Christl, M., & Vockenhuber, C. (2021). Deciphering the evolution of the Bleis Marscha rock glacier (Val d'Err, eastern Switzerland) with cosmogenic nuclide exposure dating, aerial image correlation, and finite element modeling. *Cryosphere*, *15*(4), 2057–2081. https://doi.org/10.5194/tc-15-2057-2021

Anderson, R. S., Anderson, L. S., Armstrong, W. H., Rossi, M. W., & Crump, S. E. (2018). Glaciation of alpine valleys: The glacier–debris-covered glacier–rock glacier continuum. *Geomorphology*, *311*, 127–142. https://doi.org/10.1016/j.geomorph.2018.03.015

Andrés, N., Gómez-Ortiz, A., Fernández-Fernández, J. M., Tanarro, L. M., Salvador-Franch, F., Oliva, M., & Palacios, D. (2018). Timing of deglaciation and rock glacier origin in the southeastern Pyrenees: a review and new data. *Boreas*, *47*(4), 1050–1071. https://doi.org/10.1111/bor.12324

Balco, G., Stone, J. O., Lifton, N. A., & Dunai, T. J. (2008). A complete and easily accessible means of calculating surface exposure ages or erosion rates from ^{10}Be and ^{26}Al measurements. *Quaternary Geochronology*, *3*(3), 174–195. https://doi.org/10.1016/j.quageo.2007.12.001

Barboux, C., Delaloye, R., & Lambiel, C. (2014). Inventorying slope movements in an Alpine environment using DInSAR. *Earth Surface Processes and Landforms*, *39*(15), 2087–2099. https://doi.org/10.1002/esp.3603

Barsch, D. (1977). Nature And Importance Of Mass-Wasting By Rock Glaciers In Alpine Permafrost Environments. *Earth Surf Process*, *2*(2–3), 231–245. https://doi.org/10.1002/esp.3290020213

Berthling, I. (2011a). Beyond confusion: Rock glaciers as cryo-conditioned landforms. *Geomorphology*, *131*(3–4), 98–106. https://doi.org/10.1016/j.geomorph.2011.05.002

Berthling, I. (2011b). Beyond confusion: Rock glaciers as cryo-conditioned landforms. *Geomorphology*, *131*(3–4), 98–106. https://doi.org/10.1016/j.geomorph.2011.05.002

570 Blöthe, J. H., Halla, C., Schwalbe, E., Bottegal, E., Trombotto Liaudat, D., & Schrott, L. (2021). Surface velocity fields of active rock glaciers and ice-debris complexes in the Central Andes of Argentina. *Earth Surface Processes and Landforms*, *46*(2), 504–522. https://doi.org/10.1002/esp.5042

Bodin, X. (2013). Present status and development of rock glacier complexes in south-faced valleys (45°N, French Alps). *Geografia Fisica e Dinamica Quaternaria*, *36*(1), 27–38. https://doi.org/10.4461/GFDQ.2013.36.2

575 Bodin, X., Thibert, E., Sanchez, O., Rabatel, A., & Jaillet, S. (2018). Multi-Annual kinematics of an active rock glacier quantified from very high-resolution DEMs: An application-case in the French Alps. *Remote Sensing*, *10*(4). https://doi.org/10.3390/rs10040547

Böhlert, R., Compeer, M., Egli, M., Brandová, D., Maisch, M., Kubik, P. W., & Haeberli, W. (2011). A combination of relative-numerical dating methods indicates two high alpine rock glacier activity phases after the glacier advance of the
580 younger dryas. *Open Geography Journal*, *4*, 115–130. https://doi.org/10.2174/1874923201104010115

Braucher, R., Bourlès, D., Merchel, S., … J. R.-N. I. and, & 2013, undefined. (n.d.). Determination of muon attenuation lengths in depth profiles from in situ produced cosmogenic nuclides. *Elsevier*. Retrieved December 13, 2021, from https://www.sciencedirect.com/science/article/pii/S0168583X12002911

Brown, E. T., Edmond, J. M., Raisbeck, G. M., Yiou, F., Kurz, M. D., & Brook, E. J. (1991). Examination of surface exposure
585 ages of Antarctic moraines using in situ produced [10]Be and [26]Al. *Geochimica et Cosmochimica Acta*, *55*(8), 2269–2283. https://doi.org/10.1016/0016-7037(91)90103-C

Charton, J., Verfaillie, D., Jomelli, V., & Francou, B. (2021). Early Holocene rock glacier stabilisation at col du Lautaret (French Alps): Palaeoclimatic implications. *Geomorphology*, *394*. https://doi.org/10.1016/j.geomorph.2021.107962

Chenet, M., Brunstein, D., Jomelli, V., Roussel, E., Rinterknecht, V., Mokadem, F., Biette, M., Robert, V., & Léanni, L.
590 (2016). [10]Be cosmic-ray exposure dating of moraines and rock avalanches in the Upper Romanche valley (French Alps): Evidence of two glacial advances during the Late Glacial/Holocene transition. *Quaternary Science Reviews*, *148*, 209–221. https://doi.org/10.1016/j.quascirev.2016.07.025

Claude, A., Ivy-Ochs, S., Kober, F., Antognini, M., Salcher, B., & Kubik, P. W. (2014). The Chironico landslide (Valle Leventina, southern Swiss Alps): age and evolution. *Swiss Journal of Geosciences*, *107*(2–3), 273–291.
595 https://doi.org/10.1007/s00015-014-0170-z

Cossart, E., Fort, M., Bourles, D., Carcaillet, J., Perrier, R., Siame, L., & Braucher, R. (2010a). Climatic significance of glacier retreat and rockglaciers re-assessed in the light of cosmogenic dating and weathering rind thickness in Clarée valley (Briançonnais, French Alps). *Catena*, *80*(3), 204–219. https://doi.org/10.1016/j.catena.2009.11.007

600 Cossart, E., Fort, M., Bourles, D., Carcaillet, J., Perrier, R., Siame, L., & Braucher, R. (2010b). Climatic significance of glacier retreat and rockglaciers re-assessed in the light of cosmogenic dating and weathering rind thickness in Clarée valley (Briançonnais, French Alps). *Catena*, *80*(3), 204–219. https://doi.org/10.1016/j.catena.2009.11.007

Coûteaux, M., & Edouard, J.-L. (1987). La déglaciation du site du lac des Bèches (Massif des Ecrins). Etude pollenanalytique et glacio-morphologique. *Revue de Géographie Alpine*, *75*(1), 63–77. https://doi.org/10.3406/rga.1987.2666

605 Cremonese, E., Gruber, S., Phillips, M., Pogliotti, P., Boeckli, L., Noetzli, J., Suter, C., Bodin, X., Crepaz, A., Kellerer-Pirklbauer, A., Lang, K., Letey, S., Mair, V., Morra Di Cella, U., Ravanel, L., Scapozza, C., Seppi, R., & Zischg, A. (2011). Brief communication: "An inventory of permafrost evidence for the European Alps." *Cryosphere*, *5*(3), 651–657. https://doi.org/10.5194/tc-5-651-2011

Cusicanqui, D., Rabatel, A., & Vincent, C. (2021). *Interpretation of Volume and Flux Changes of the Laurichard Rock Glacier*
610 *Between 1952 and 2019 , French Alps Journal of Geophysical Research : Earth Surface.* https://doi.org/10.1029/2021JF006161

Cusicanqui, D., Rabatel, A., Vincent, C., Bodin, X., Thibert, E., & Francou, B. (2021a). Interpretation of Volume and Flux Changes of the Laurichard Rock Glacier Between 1952 and 2019, French Alps. *Journal of Geophysical Research: Earth Surface*, *126*(9), e2021JF006161. https://doi.org/10.1029/2021JF006161

Cusicanqui, D., Rabatel, A., Vincent, C., Bodin, X., Thibert, E., & Francou, B. (2021b). Interpretation of Volume and Flux
615 Changes of the Laurichard Rock Glacier Between 1952 and 2019, French Alps. *Journal of Geophysical Research: Earth Surface*, *126*(9), e2021JF006161. https://doi.org/10.1029/2021JF006161

Dall'Asta, E., Forlani, G., Roncella, R., Santise, M., Diotri, F., & Morra di Cella, U. (2017). Unmanned Aerial Systems and DSM matching for rock glacier monitoring. *ISPRS Journal of Photogrammetry and Remote Sensing*, *127*, 102–114. https://doi.org/10.1016/j.isprsjprs.2016.10.003

620 Delaloye, R., & Echelard, T. (2020). IPA Action Group Rock glacier inventories and kinematics (version 4.1). *International Permafrost Association*, 1–13.

Delaloye, R., Lambiel, C., & Gärtner-Roer, I. (2010). Aperçu de la cinématique des glaciers rocheux dans les alpes suisses. Rythme saisonnier, variations interannuelles et tendance pluri-décennale. *Geographica Helvetica*, *65*(2), 135–145. https://doi.org/10.5194/gh-65-135-2010

625 Delunel, R. (2010). Evolution géomorphologique du massif des Ecrins-Pelvoux depuis le Dernier Maximum Glaciaire – Apports des nucléides cosmogéniques produits in-situ. *Ecole Doctorale Terre Univers Environnement Laboratoire de Géodynamique Des Chaînes Alpines*, *Ph. D. The*, 236.

Delunel, Romain, Bourlès, D. L., van der Beek, P. A., Schlunegger, F., Leya, I., Masarik, J., & Paquet, E. (2014). Snow

shielding factors for cosmogenic nuclide dating inferred from long-term neutron detector monitoring. *Quaternary Geochronology*, *24*, 16–26. https://doi.org/10.1016/j.quageo.2014.07.003

Delunel, Romain, van der Beek, P. A., Carcaillet, J., Bourlès, D. L., & Valla, P. G. (2010). Frost-cracking control on catchment denudation rates: Insights from in situ produced [10]Be concentrations in stream sediments (Ecrins-Pelvoux massif, French Western Alps). *Earth and Planetary Science Letters*, *293*(1–2), 72–83. https://doi.org/10.1016/j.epsl.2010.02.020

Eriksen, H., Rouyet, L., Lauknes, T. R., Berthling, I., Isaksen, K., Hindberg, H., Larsen, Y., & Corner, G. D. (2018). Recent Acceleration of a Rock Glacier Complex, Adjet, Norway, Documented by 62 Years of Remote Sensing Observations. *Geophysical Research Letters*, *45*(16), 8314–8323. https://doi.org/10.1029/2018GL077605

Federici, P. R., Granger, D. E., Pappalardo, M., Ribolino, A., Spagnolo, M., & Cyr, A. J. (2008). Exposure age dating and Equilibrium Line Altitude reconstruction of an Egesen moraine in the Maritime Alps, Italy. *Boreas*, *37*(2), 245–253. https://doi.org/10.1111/j.1502-3885.2007.00018.x

Fernández-Fernández, J. M., Palacios, D., Andrés, N., Schimmelpfennig, I., Tanarro, L. M., Brynjólfsson, S., López-Acevedo, F. J., Sæmundsson, Þ., & Team, A. S. T. E. R. (2020). Constraints on the timing of debris-covered and rock glaciers: An exploratory case study in the Hólar area, northern Iceland. *Geomorphology*, *361*, 107196. https://doi.org/10.1016/j.geomorph.2020.107196

Francou, B. (1982). Chutes de pierres et éboulisation dans les parois de l'étage périglaciaire. *Revue de Géographie Alpine*, *70*(3), 279–300. https://doi.org/10.3406/rga.1982.2508

Francou, B., & Reynaud, L. (1992). 10 year surficial velocities on a rock glacier (Laurichard, French Alps). *Permafrost and Periglacial Processes*, *3*(3), 209–213. https://doi.org/10.1002/ppp.3430030306

Frehner, M., Ling, A. H. M., & Gärtner-Roer, I. (2015). Furrow-and-ridge morphology on rockglaciers explained by gravity-driven buckle folding: A case study from the murtèl rockglacier (Switzerland). *Permafrost and Periglacial Processes*, *26*(1), 57–66. https://doi.org/10.1002/ppp.1831

Fuchs, M. C., Böhlert, R., Krbetschek, M., Preusser, F., & Egli, M. (2013). Exploring the potential of luminescence methods for dating Alpine rock glaciers. *Quaternary Geochronology*, *18*, 17–33. https://doi.org/10.1016/j.quageo.2013.07.001

Gallach, X., Carcaillet, J., Ravanel, L., Deline, P., Ogier, C., Rossi, M., Malet, E., & Garcia-Sellés, D. (2020). Climatic and structural controls on Late-glacial and Holocene rockfall occurrence in high-elevated rock walls of the Mont Blanc massif (Western Alps). *Earth Surface Processes and Landforms*, *45*(13), 3071–3091. https://doi.org/10.1002/esp.4952

Gallach, X., Ravanel, L., Egli, M., Brandova, D., Schaepman, M., Christl, M., Gruber, S., Deline, P., Carcaillet, J., & Pallandre, F. (2018). Timing of rockfalls in the Mont Blanc massif (Western Alps): evidence from surface exposure dating with

cosmogenic [10]Be. *Landslides*, *15*(10), 1991–2000. https://doi.org/10.1007/s10346-018-0999-8

Gardent, M., Rabatel, A., Dedieu, J. P., & Deline, P. (2014). Multitemporal glacier inventory of the French Alps from the late
660   1960s to the late 2000s. *Global and Planetary Change*, *120*, 24–37. https://doi.org/10.1016/j.gloplacha.2014.05.004

Giardino, J. R., & Vitek, J. D. (1988). The significance of rock glaciers in the glacial-periglacial landscape continuum. *Journal
of Quaternary Science*, *3*(1), 97–103. https://doi.org/10.1002/jqs.3390030111

Gosse, J. C., & Phillips, F. M. (2001). Terrestrial in situ cosmogenic nuclides: Theory and application. *Quaternary Science
Reviews*, *20*(14), 1475–1560. https://doi.org/10.1016/S0277-3791(00)00171-2

665 Haeberli, W. (2013). Mountain permafrost - research frontiers and a special long-term challenge. *Cold Regions Science and
Technology*, *96*, 71–76. https://doi.org/10.1016/j.coldregions.2013.02.004

Haeberli, W., Hallet, B., Arenson, L., Elconin, R., Humlum, O., Kääb, A., Kaufmann, V., Ladanyi, B., Matsuoka, N.,
Springman, S., & Mühll, D. V. (2006). Permafrost creep and rock glacier dynamics. *Permafrost and Periglacial
Processes*, *17*(3), 189–214. https://doi.org/10.1002/ppp.561

670 Hippolyte, J. C., Bourlès, D., Braucher, R., Carcaillet, J., Léanni, L., Arnold, M., & Aumaitre, G. (2009). Cosmogenic [10]Be
dating of a sackung and its faulted rock glaciers, in the Alps of Savoy (France). *Geomorphology*, *108*(3–4), 312–320.
https://doi.org/10.1016/j.geomorph.2009.02.024

Hormes, A., Ivy-Ochs, S., Kubik, P. W., Ferreli, L., & Maria Michetti, A. (2008). [10]Be exposure ages of a rock avalanche and
a late glacial moraine in Alta Valtellina, Italian Alps. *Quaternary International*, *190*(1), 136–145.
675   https://doi.org/10.1016/j.quaint.2007.06.036

Ikeda, A., Matsuoka, N., & Kääb, A. (2008). Fast deformation of perennially frozen debris in a warm rock glacier in the Swiss
Alps: An effect of liquid water. *Journal of Geophysical Research: Earth Surface*, *113*(1).
https://doi.org/10.1029/2007JF000859

Ivy-Ochs, S. (2015). Variaciones glaciares en los Alphs europoes al final de la última glaciación. *Cuadernos de Investigacion
680   Geografica*, *41*(2), 295–315. https://doi.org/10.18172/cig.2750

Ivy-Ochs, Susan, Kerschner, H., Kubik, P. W., & Schlüchter, C. (2006). Glacier response in the European Alps to Heinrich
Event 1 cooling: The Gschnitz stadial. In *Journal of Quaternary Science* (Vol. 21, Issue 2, pp. 115–130).
https://doi.org/10.1002/jqs.955

Ivy-Ochs, Susan, Kerschner, H., Reuther, A., Preusser, F., Heine, K., Maisch, M., Kubik, P. W., & Schlüchter, C. (2008).

685   Chronology of the last glacial cycle in the European Alps. *Journal of Quaternary Science*, *23*(6–7), 559–573. https://doi.org/10.1002/jqs.1202

Jones, D. B., Harrison, S., Anderson, K., & Whalley, W. B. (2019). Rock glaciers and mountain hydrology: A review. *Earth-Science Reviews*, *193*(March), 66–90. https://doi.org/10.1016/j.earscirev.2019.04.001

Kaab, A., Haeberli, W., & Hilmar Gudmundsson, G. (1997). Analysing the creep of mountain permafrost using high precision
690   aerial photogrammetry: 25 years of monitoring Gruben rock glacier, Swiss Alps. *Permafrost and Periglacial Processes*, *8*(4), 409–426. https://doi.org/10.1002/(SICI)1099-1530(199710/12)8:4<409::AID-PPP267>3.0.CO;2-C

Kellerer-Pirklbauer, A. (2017). Potential weathering by freeze-thaw action in alpine rocks in the European Alps during a nine year monitoring period. *Geomorphology*, *296*, 113–131. https://doi.org/10.1016/j.geomorph.2017.08.020

Kellerer-Pirklbauer, A., & Rieckh, M. (2016). Monitoring nourishment processes in the rooting zone of an active rock glacier
695   in an alpine environment. *Zeitschrift Fur Geomorphologie*, *60*, 99–121. https://doi.org/10.1127/zfg_suppl/2016/00245

Kelly, M. A., Buoncristiani, J. F., & Schlüchter, C. (2004). A reconstruction of the last glacial maximum (LGM) ice-surface geometry in the western Swiss Alps and contiguous Alpine regions in Italy and France. *Eclogae Geologicae Helvetiae*, *97*(1), 57–75. https://doi.org/10.1007/s00015-004-1109-6

Kenner, R., Phillips, M., Limpach, P., Beutel, J., & Hiller, M. (2018). Monitoring mass movements using georeferenced time-
700   lapse photography: Ritigraben rock glacier, western Swiss Alps. *Cold Regions Science and Technology*, *145*, 127–134. https://doi.org/10.1016/j.coldregions.2017.10.018

Kohl, C. P., & Nishiizumi, K. (1992). Chemical isolation of quartz for measurement of in-situ -produced cosmogenic nuclides. In *Geochimica et Cosmochimica Acta* (Vol. 56, Issue 9, pp. 3583–3587). Pergamon. https://doi.org/10.1016/0016-7037(92)90401-4

705 Krainer, K., Bressan, D., Dietre, B., Haas, J. N., Hajdas, I., Lang, K., Mair, V., Nickus, U., Reidl, D., Thies, H., & Tonidandel, D. (2015). A 10,300-year-old permafrost core from the active rock glacier Lazaun, southern Ötztal Alps (South Tyrol, northern Italy). *Quaternary Research (United States)*, *83*(2), 324–335. https://doi.org/10.1016/j.yqres.2014.12.005

Le Roy, M., Deline, P., Carcaillet, J., Schimmelpfennig, I., & Ermini, M. (2017). [10]Be exposure dating of the timing of Neoglacial glacier advances in the Ecrins-Pelvoux massif, southern French Alps. *Quaternary Science Reviews*,
710   *178*(December), 118–138. https://doi.org/10.1016/j.quascirev.2017.10.010

Lifton, N., Sato, T., & Dunai, T. J. (2014). Scaling in situ cosmogenic nuclide production rates using analytical approximations to atmospheric cosmic-ray fluxes. *Earth and Planetary Science Letters*, *386*, 149–160. https://doi.org/10.1016/j.epsl.2013.10.052

Liu, L., Millar, C. I., Westfall, R. D., & Zebker, H. A. (2013). Surface motion of active rock glaciers in the Sierra Nevada, California, USA: Inventory and a case study using InSAR. *Cryosphere*, *7*(4), 1109–1119. https://doi.org/10.5194/tc-7-1109-2013

Marcer, M., Cicoira, A., Cusicanqui, D., Bodin, X., Echelard, T., Obregon, R., & Schoeneich, P. (2021). Rock glaciers throughout the French Alps accelerated and destabilised since 1990 as air temperatures increased. *Communications Earth & Environment*, *2*(1), 1–11. https://doi.org/10.1038/s43247-021-00150-6

Martin, L. C. P., Blard, P. H., Balco, G., Lavé, J., Delunel, R., Lifton, N., & Laurent, V. (2017). The CREp program and the ICE-D production rate calibration database: A fully parameterizable and updated online tool to compute cosmic-ray exposure ages. *Quaternary Geochronology*, *38*, 25–49. https://doi.org/10.1016/j.quageo.2016.11.006

Matthews, J. A., & Wilson, P. (2015). Improved Schmidt-hammer exposure ages for active and relict pronival ramparts in southern Norway, and their palaeoenvironmental implications. *Geomorphology*, *246*, 7–21. https://doi.org/10.1016/j.geomorph.2015.06.002

Merchel, S., & Herpers, U. (1999). An update on radiochemical separation techniques for the determination of long-lived radionuclides via accelerator mass spectrometry. *Radiochimica Acta*, *84*(4), 215–219. https://doi.org/10.1524/ract.1999.84.4.215

Micheletti, N., Tonini, M., & Lane, S. N. (2017). Geomorphological activity at a rock glacier front detected with a 3D density-based clustering algorithm. *Geomorphology*, *278*, 287–297. https://doi.org/10.1016/j.geomorph.2016.11.016

Monegato, G., Scardia, G., Hajdas, I., Rizzini, F., & Piccin, A. (2017). The Alpine LGM in the boreal ice-sheets game. *Scientific Reports*, *7*(1), 1–8. https://doi.org/10.1038/s41598-017-02148-7

Moran, A. P., Ivy-Ochs, S., Schuh, M., Christl, M., & Kerschner, H. (2016). Evidence of central Alpine glacier advances during the Younger Dryas–early Holocene transition period. *Boreas*, *45*(3), 398–410. https://doi.org/10.1111/bor.12170

Necsoiu, M., Onaca, A., Wigginton, S., & Urdea, P. (2016). Rock glacier dynamics in Southern Carpathian Mountains from high-resolution optical and multi-temporal SAR satellite imagery. *Remote Sensing of Environment*, *177*, 21–36. https://doi.org/10.1016/j.rse.2016.02.025

Nuth, C., & Kääb. (2011). Co-registration and bias corrections of satellite elevation data sets for quantifying glacier thickness change. *Cryosphere*, *5*(1), 271–290. https://doi.org/10.5194/tc-5-271-2011

Paasche, Ø., Dahl, S. O., Løvlie, R., Bakke, J., & Nesje, A. (2007). Rockglacier activity during the Last Glacial-Interglacial transition and Holocene spring snowmelting. *Quaternary Science Reviews*, *26*(5–6), 793–807. https://doi.org/10.1016/j.quascirev.2006.11.017

Palacios, D., Oliva, M., Gómez-Ortiz, A., Andrés, N., Fernández-Fernández, J. M., Schimmelpfennig, I., Léanni, L., & Team, A. S. T. E. R. (2020). Climate sensitivity and geomorphological response of cirque glaciers from the late glacial to the Holocene, Sierra Nevada, Spain. *Quaternary Science Reviews*, *248*. https://doi.org/10.1016/j.quascirev.2020.106617

Pavón-Carrasco, F. J., Osete, M. L., Torta, J. M., & De Santis, A. (2014). A geomagnetic field model for the Holocene based on archaeomagnetic and lava flow data. *Earth and Planetary Science Letters*, *388*, 98–109. https://doi.org/10.1016/j.epsl.2013.11.046

Protin, M., Schimmelpfennig, I., Mugnier, J. L., Ravanel, L., Le Roy, M., Deline, P., Favier, V., Buoncristiani, J. F., Aumaître, G., Bourlès, D. L., & Keddadouche, K. (2019). Climatic reconstruction for the Younger Dryas/Early Holocene transition and the Little Ice Age based on paleo-extents of Argentière glacier (French Alps). *Quaternary Science Reviews*, *221*. https://doi.org/10.1016/j.quascirev.2019.105863

RGIK. (2020). *Rock glacier inventory using InSAR (kinematic approach), Practical Guidelines v3.0.2*. https://bigweb.unifr.ch/Science/Geosciences/Geomorphology/Pub/Website/CCI/CurrentVersion/Current_InSAR-based_Guidelines.pdf

Robson, B. A., Bolch, T., MacDonell, S., Hölbling, D., Rastner, P., & Schaffer, N. (2020). Automated detection of rock glaciers using deep learning and object-based image analysis. *Remote Sensing of Environment*, *250*, 112033. https://doi.org/10.1016/j.rse.2020.112033

Rodríguez-Rodríguez, L., Jiménez-Sánchez, M., Domínguez-Cuesta, M. J., Rinterknecht, V., & Pallàs, R. (2017). Timing of last deglaciation in the Cantabrian Mountains (Iberian Peninsula; North Atlantic Region) based on in situ-produced [10]Be exposure dating. *Quaternary Science Reviews*, *171*, 166–181. https://doi.org/10.1016/j.quascirev.2017.07.012

Sandeman, A. F., & Ballantyne, C. K. (1996). Talus rock glaciers in scotland: Characteristics and controls on formation. *Scottish Geographical Magazine*, *112*(3), 138–146. https://doi.org/10.1080/14702549608554947

Scambos, T. A., Dutkiewicz, M. J., Wilson, J. C., & Bindschadler, R. A. (1992). Application of image cross-correlation to the measurement of glacier velocity using satellite image data. *Remote Sensing of Environment*, *42*(3), 177–186. https://doi.org/10.1016/0034-4257(92)90101-O

Scapozza, C., Lambiel, C., Bozzini, C., Mari, S., & Conedera, M. (2014). Assessing the rock glacier kinematics on three different timescales: A case study from the southern Swiss Alps. *Earth Surface Processes and Landforms*, *39*(15), 2056–2069. https://doi.org/10.1002/esp.3599

Schimmelpfennig, I., Schaefer, J. M., Akçar, N., Koffman, T., Ivy-Ochs, S., Schwartz, R., Finkel, R. C., Zimmerman, S., & Schlüchter, C. (2014). A chronology of Holocene and Little Ice Age glacier culminations of the Steingletscher, Central Alps, Switzerland, based on high-sensitivity beryllium-10 moraine dating. *Earth and Planetary Science Letters*, *393*, 220–230. https://doi.org/10.1016/j.epsl.2014.02.046

Schindelwig, I., Akçar, N., Kubik, P. W., & Schlüchter, C. (2012). Lateglacial and early Holocene dynamics of adjacent valley
glaciers in the Western Swiss Alps. *Journal of Quaternary Science*, *27*(1), 114–124. https://doi.org/10.1002/jqs.1523

Shean, D. E., Alexandrov, O., Moratto, Z. M., Smith, B. E., Joughin, I. R., Porter, C., & Morin, P. (2016). An automated,
open-source pipeline for mass production of digital elevation models (DEMs) from very-high-resolution commercial
stereo satellite imagery. *ISPRS Journal of Photogrammetry and Remote Sensing*, *116*, 101–117.
https://doi.org/10.1016/j.isprsjprs.2016.03.012

Steinemann, O., Reitner, J. M., Ivy-Ochs, S., Christl, M., & Synal, H. A. (2020). Tracking rockglacier evolution in the Eastern
Alps from the Lateglacial to the early Holocene. *Quaternary Science Reviews*, *241*.
https://doi.org/10.1016/j.quascirev.2020.106424

Strozzi, T., Caduff, R., Jones, N., Barboux, C., Delaloye, R., Bodin, X., Kääb, A., Mätzler, E., & Schrott, L. (2020). Monitoring
Rock Glacier Kinematics with Satellite Synthetic Aperture Radar. *Remote Sensing*, *12*(3), 559.
https://doi.org/10.3390/rs12030559

Thibert, E., Bodin, X., Bonnefoy-Demongeot, M., & Finance, F. (2018). Extracting the time signal in surface velocity changes
along 3 decades at Laurichard rock glacier (French Alps). In *researchgate.net*.
https://www.researchgate.net/publication/326648894

Uppala, S. M., Kållberg, P. W., Simmons, A. J., Andrae, U., Bechtold, V. D. C., Fiorino, M., Gibson, J. K., Haseler, J.,
Hernandez, A., Kelly, G. A., Li, X., Onogi, K., Saarinen, S., Sokka, N., Allan, R. P., Andersson, E., Arpe, K., Balmaseda,
M. A., Beljaars, A. C. M., … Woollen, J. (2005). The ERA-40 re-analysis. *Quarterly Journal of the Royal
Meteorological Society*, *131*(612), 2961–3012. https://doi.org/10.1256/qj.04.176

Valla, P. G., van der Beek, P. A., & Carcaillet, J. (2010). Dating bedrock gorge incision in the French Western Alps (Ecrins-
Pelvoux massif) using cosmogenic ^{10}Be. *Terra Nova*, *22*(1), 18–25. https://doi.org/10.1111/j.1365-3121.2009.00911.x

Vivero, S., & Lambiel, C. (2019). Monitoring the crisis of a rock glacier with repeated UAV surveys. *Geographica Helvetica*,
74(1), 59–69. https://doi.org/10.5194/gh-74-59-2019

Wahrhaftig, C., & Cox, A. (1959). Rock glaciers in the Alaska Range. *Bulletin of the Geological Society of America*, *70*(4),
383–436. https://doi.org/10.1130/0016-7606(1959)70[383:RGITAR]2.0.CO;2

Whalley, W. B. (1974). Origin of rock glaciers. *Journal of Glaciology*, *13*(68), 323–324.
https://doi.org/10.3189/s0022143000023145

Williams, M. W., Knauf, M., Caine, N., Liu, F., & Verplanck, P. L. (2006). Geochemistry and source waters of rock glacier
outflow, Colorado Front Range. *Permafrost and Periglacial Processes*, *17*(1), 13–33. https://doi.org/10.1002/ppp.535

Winkler, S., & Lambiel, C. (2018). Age constraints of rock glaciers in the Southern Alps/New Zealand – Exploring their palaeoclimatic potential. *Holocene*, *28*(5), 778–790. https://doi.org/10.1177/0959683618756802

805   Wirsig, C., Zasadni, J., Ivy-Ochs, S., Christl, M., Kober, F., & Schlüchter, C. (2016). A deglaciation model of the Oberhasli, Switzerland. *Journal of Quaternary Science*, *31*(1), 46–59. https://doi.org/10.1002/jqs.2831

Wirz, V., Gruber, S., Purves, R. S., Beutel, J., Gärtner-Roer, I., Gubler, S., & Vieli, A. (2016). Short-term velocity variations at three rock glaciers and their relationship with meteorological conditions. *Earth Surface Dynamics*, *4*(1), 103–123. https://doi.org/10.5194/esurf-4-103-2016

810
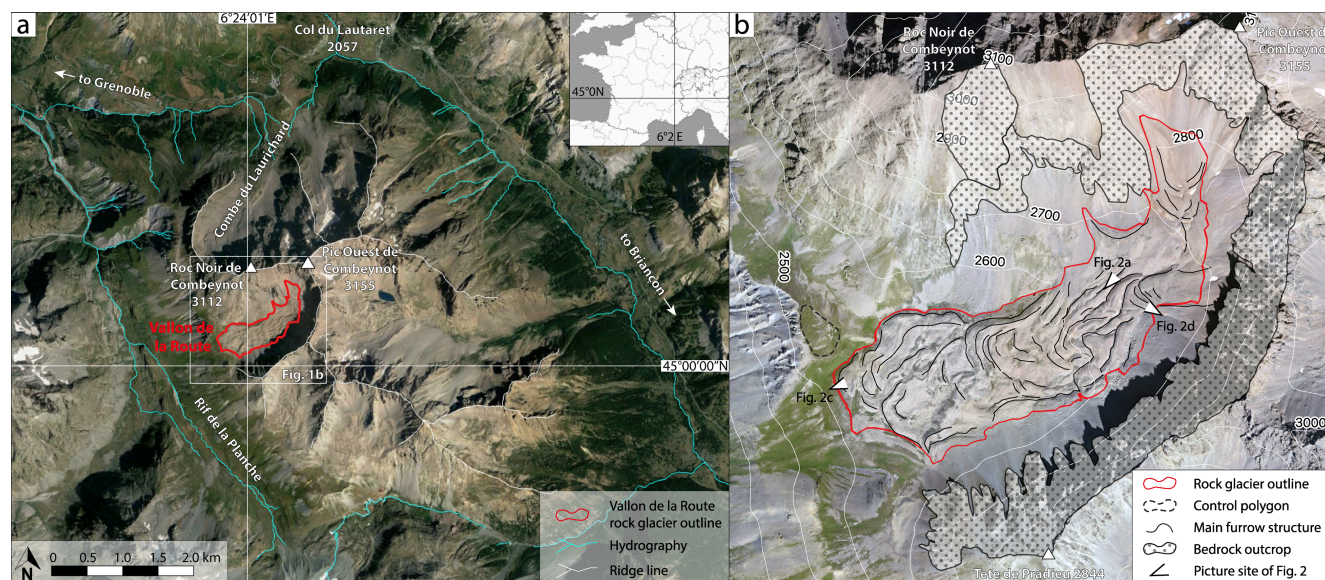
Figure 1: a. Regional map of the Combeynot massif showing the Vallon de la Route rock-glacier and surrounding topography (Satellite image from © Google Earth 2020). Outline of the rock glacier (red), hydrography (cyan) and ridge line (white) from Bodin
815   **(2007). Inset show location of the Vallon de la Route rock glacier within western Europe b. Map of the Vallon de la Route rock glacier, with outline of the rock glacier, main furrow structures, outline of the bedrock outcrops (from Bodin, 2007) and location/orientation of pictures presented in Figure 2. Satellite image from Bing Aerial © Microsoft.**
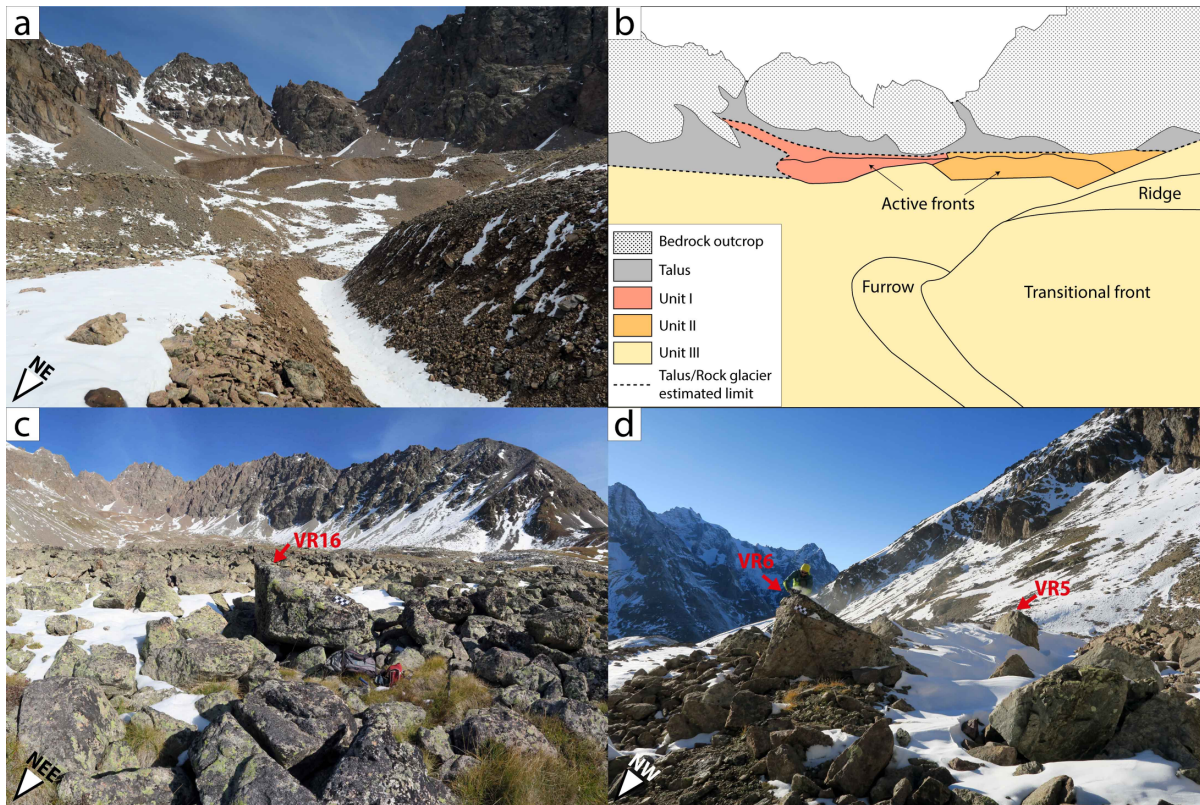
 Figure 2: a-b. Picture (a) looking toward the NE and geomorphological interpretation (b) of the rock glacier units I, II and III, with bedrock outcrops, talus, ridge, furrow and fronts. c. Picture looking toward the NEE of the relict unit V and sampled boulder (VR16). d. Picture looking toward the NW of the landform E where two different boulders were sampled (VR5 and VR6). Picture locations and orientations are indicated on Figure 1b.

Earth **Surface**
Dynamics
Discussions
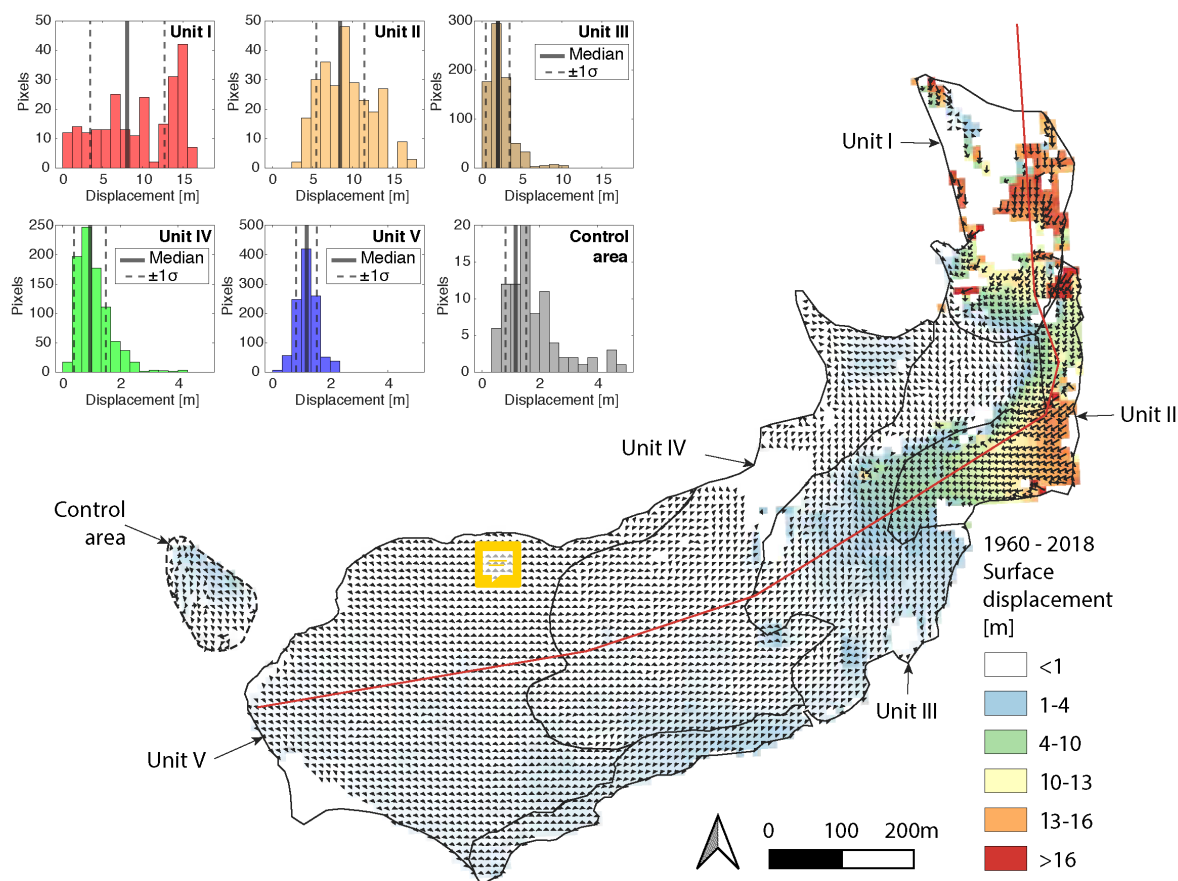
Figure 3: Surface displacement map (1960-2018) of the Vallon de la Route rock glacier. Red line is the longitudinal transect used to
825 **extract surface displacement (Fig. 4a). Black lines outline the different units of the rock-glacier system. The dashed black line**
delimits the stable terrain control area used to quantify uncertainties in the image correlation. Inset histograms (upper-left corner)
depict distribution of surface displacements within each individual unit and for the control area. Non-mapped area are the results
of the filtering process as described in Section 3.1.3.
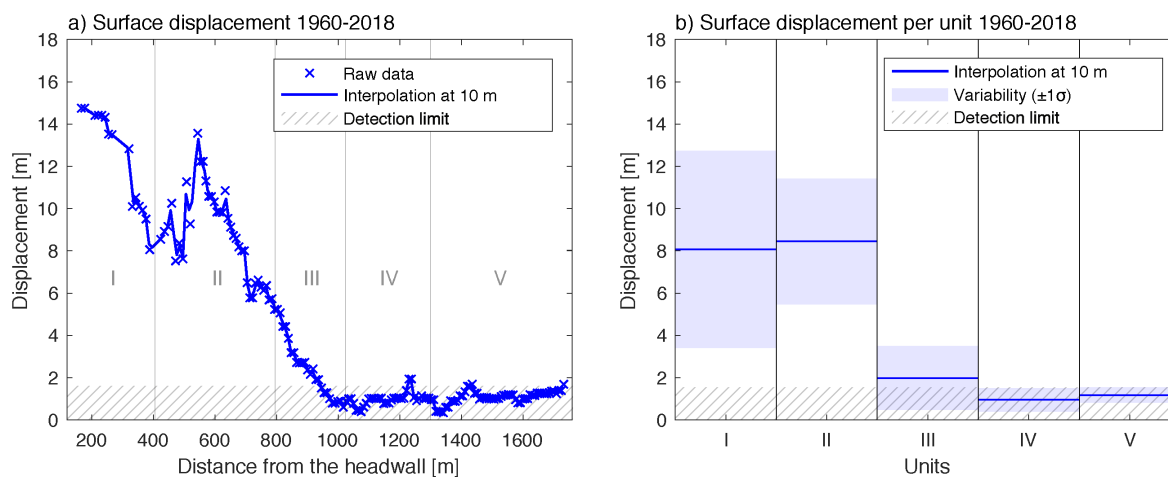
Figure 4: a. Surface displacement (1960-2018) extracted following the longitudinal transect (red line on Fig. 3) with identification of Units I to V. The blue line represents the 10-m interpolation of the raw data. b. Median surface displacement in each rock-glacier unit with its ±1σ variability (see Fig. 3 for histograms). The cross-hatched pattern represents the detection limit defined by median value of the control area (Fig. 3) used as a threshold value for detection of rock-glacier surface displacement.
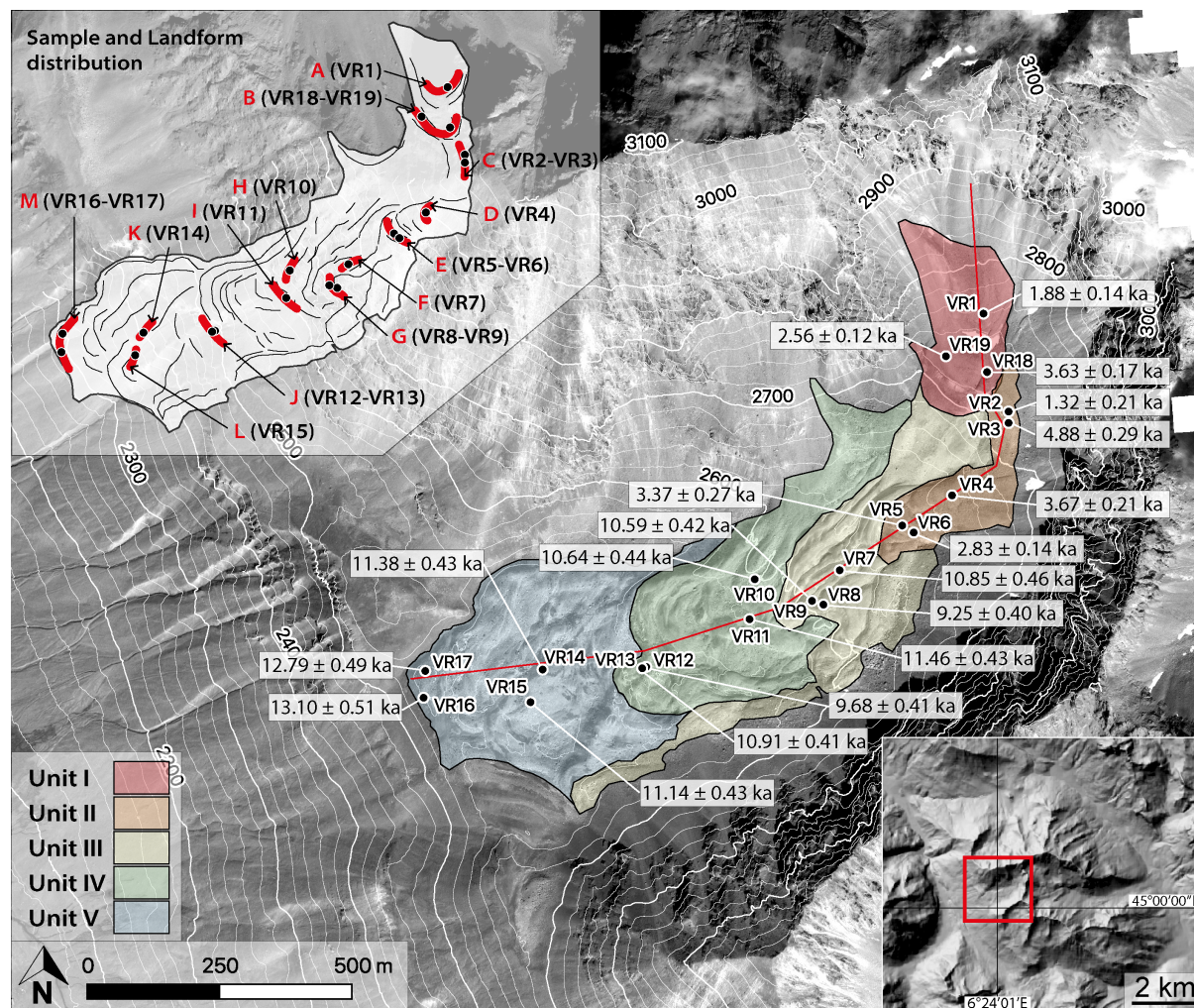
Figure 5: Map of the Vallon de la Route rock glacier, with units and sample locations. Hillshade DEM has been produced from Lidar scanning with 0.5-m resolution, white lines show elevation isolines. Red line is the longitudinal transect used to extract surface displacement (Fig. 4a). Individual ^{10}Be surface-exposure ages are shown with one standard deviation (Table 2). The lower right inset shows location of the study area within the Combeynost massif (red box). Upper left inset shows the samples (black dots) and landforms (red lines) distribution over the main furrow structures (black lines).
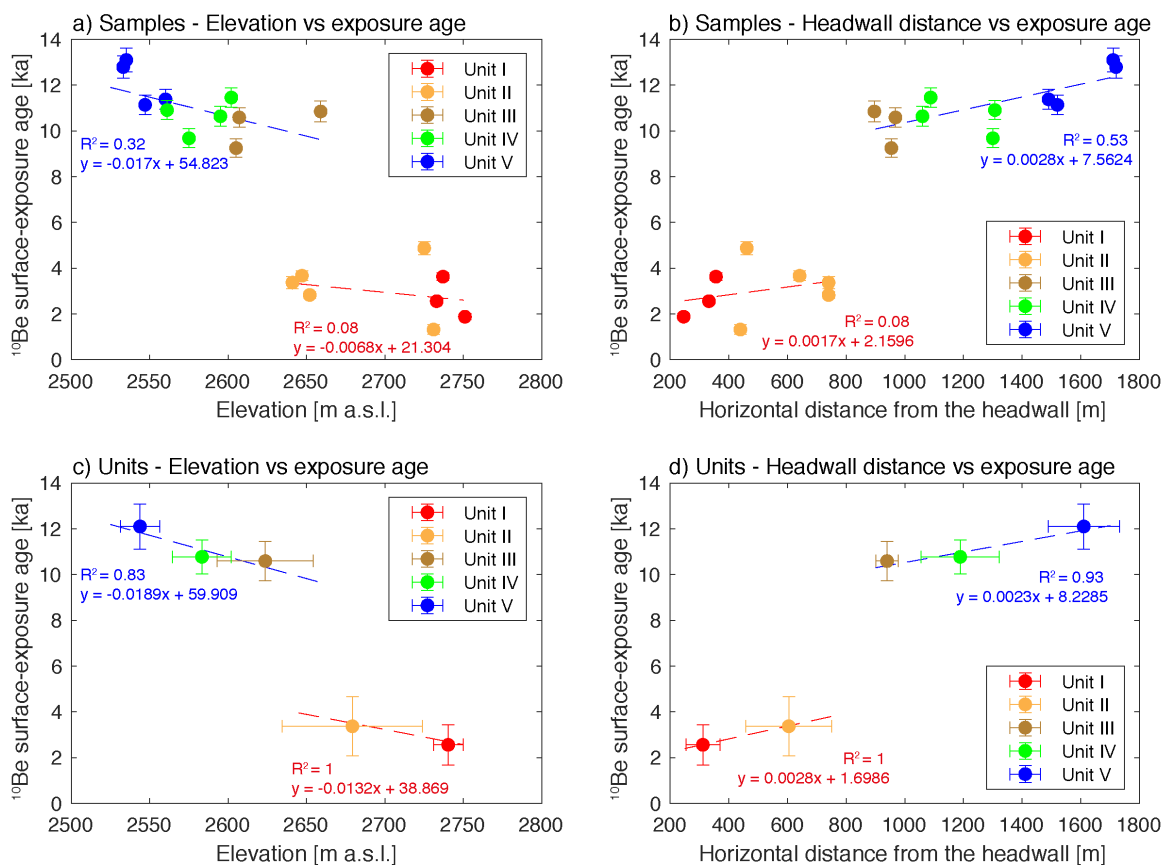
Figure 6: ^{10}**Be surface-exposure ages of individual samples (a, b) and units (c, d, median) plotted against elevation (left panels) and horizontal distance to the headwall (right panels). The red and blue dashed lines represent the linear regressions for cluster 1 (Units I and II) and 2 (Units III, IV and V), respectively. The dotted black line represents the linear regression for the entire dataset.**
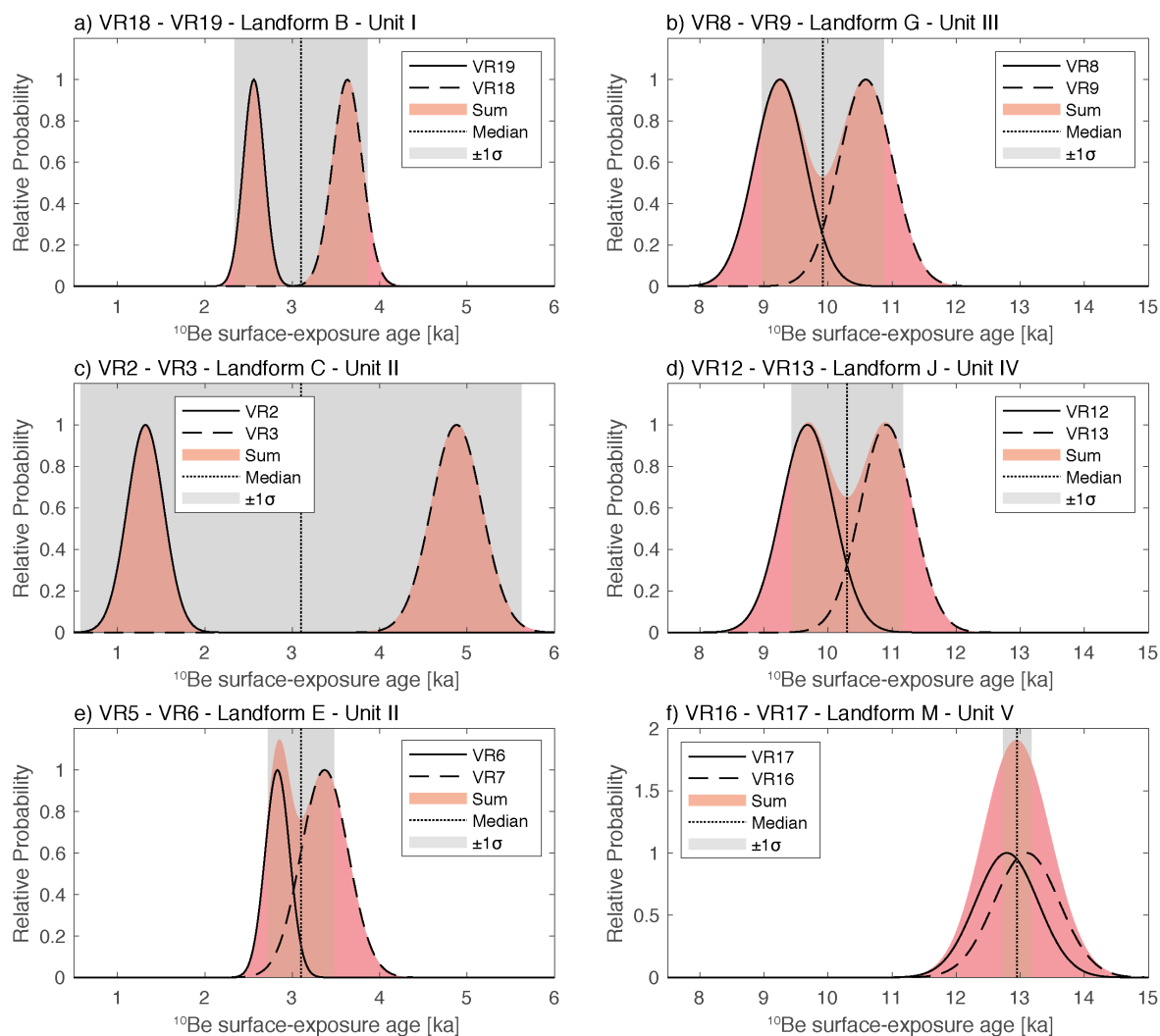
Figure 7: Probability plots of the individual ^{10}Be surface-exposure ages, sum and median for each landform (similar results in Fig. A3 for each unit in Supplementary material).
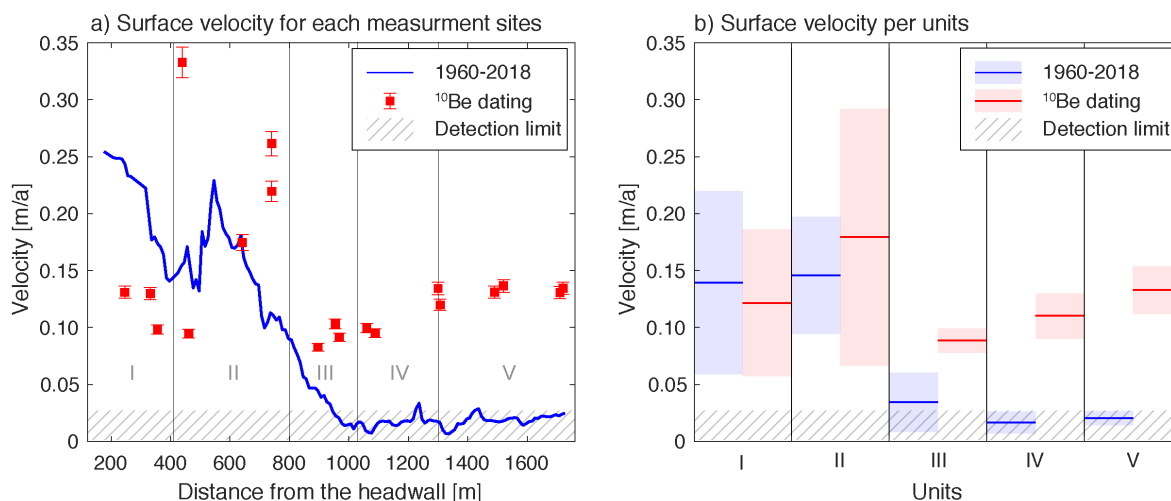
Figure 8: a. Rock-glacier surface velocity from ^{10}Be surface-exposure dating (distance from the headwall divided by the ^{10}Be surface-exposure age, red squares) and from orthoimage correlation (IMCORR, SAGA package in QGIS, 1960-2018 interval, blueline). b. Median surface velocities are presented for each independent method and each individual unit with their standard deviation (±1σ). The dashed pattern represents the detection limit (0.026 m/a) defined by median value of the control area on Figure 3 (used as a threshold value to detect rock-glacier surface movement).

a: Range of possible distance at which a fallen block is incorported in the rock glacier
b: Range of possible inheritance
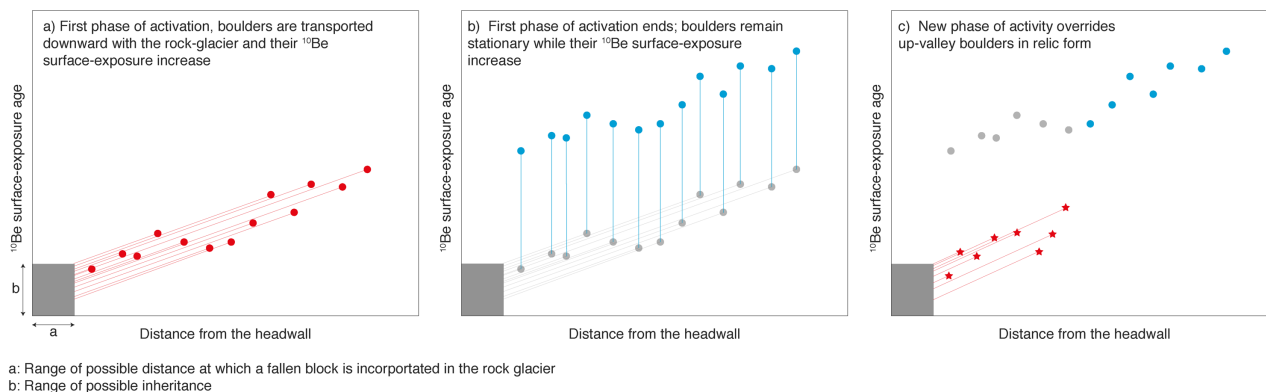
Figure 9: Schematic interpretation of the evolution of the ^{10}Be surface-exposure age patterns as a function of distance from the headwall, considering two phases of rock-glacier activity and stochastic rockfall delivery of boulders. See section 5.3 for details.
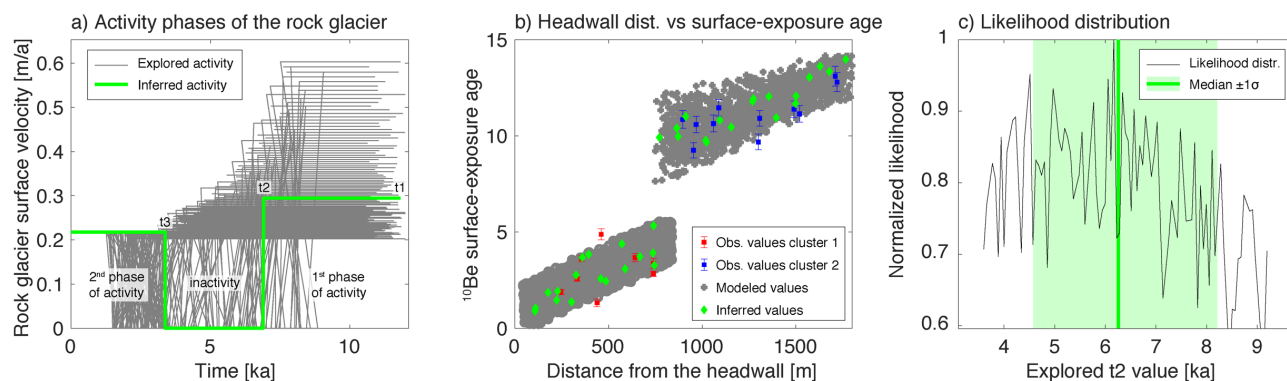
Figure 10: a) Activity phases of the rock glacier defined as the evolution of the rock glacier surface velocity in time (explored ones and best-fitting one respectively in grey and green). b) Relationship between ^{10}Be surface-exposure age and distance to the headwall. Observed values of the cluster 1 and 2, respectively in red and blue squares. Modeled and best-fitting values in grey and green respectively. c) Likelihood distribution of the inversion exploring the time at which the 1st phase of activity ends (t2). See text for details.

Table 1: Samples with geographic details within the rock-glacier system of the Vallon de la Route (Combeynot massif, France). Units are area of the rock glacier that have been defined geomorphologically. Landforms are ridges where samples have been collected, on 6 of them two replicate boulders have been sampled. The distance to the headwall has been measured following the center line of the rock glacier starting at the foot of the headwall (red line in Fig. 3, black line in Fig. 5).

Sample ID	Latitude [dec°]	Longitude [dec°]	Elevation [m a.s.l.]	Distance to the headwall [m]	Height of the sample from the ground [cm]	Unit	Landform
VR1	45.0081	6.4088	2751	246	130	I	A
VR2	45.0064	6.4093	2731	356	220	II	C
VR3	45.0063	6.4093	2725	332	230	II	C
VR4	45.0051	6.4079	2647	439	240	II	D
VR5	45.0046	6.4068	2641	461	300	II	E
VR6	45.0045	6.4069	2652	641	150	II	E
VR7	45.0039	6.4051	2659	740	240	III	F
VR8	45.0033	6.4047	2605	740	240	III	G
VR9	45.0034	6.4044	2607	896	150	III	G
VR10	45.0038	6.4031	2595	954	210	IV	H
VR11	45.0031	6.4029	2602	968	400	IV	I
VR12	45.0024	6.4004	2575	1060	320	IV	J
VR13	45.0024	6.4003	2561	1088	500	IV	J
VR14	45.0024	6.3979	2560	1300	160	V	K
VR15	45.0019	6.3976	2547	1307	400	V	L
VR16	45.0020	6.3950	2535	1490	160	V	M
VR17	45.0025	6.3951	2533	1520	180	V	M
VR18	45.0071	6.4089	2737	1710	70	I	B
VR19	45.0074	6.4079	2733	1720	100	I	B

Table 2: Sample details, analytical data related to [10]Be measurements and surface-exposure ages for the rock-glacier system of the
Vallon de la Route (Combeynot massif, France), and inputs for Crep calculator (crep.otelo.univ-lorraine.fr; Martin et al., 2017). We
used the production rate (4.16 ±0.10 at g^{-1}a^{-1}) derived by Claude et al. (2014) at the Chironico landslide site. The [10]Be surface-
exposure ages are presented with ±1σ external error and ±1σ internal error (in brackets). Shielding correction includes the
topographic shielding due to surrounding landscape and the dip of the sampled surface calculated with the online calculators
CRONUS-Earth online calculators (Balco et al., 2008, http://hess.ess.washington.edu/math). The density of the rock-boulder samples
is assumed to be 2.75 g cm^{-3}. [10]Be concentrations were corrected with blank [10]Be /[9]Be ratio of 6.28 ±0.534 ×10^{-15}. Snow-cover
correction was calculated using Gosse and Phillips (2001) equation with snow density of 0.3 g cm^{-3}, an attenuation length for fast
neutrons in snow of 150 g cm^{-2} and a cover of 50 cm of snow for 6 months of the year.

Sample ID	Thickness [cm]	Shielding factor	Quartz weight [g]	Carrier [m ^{9}Be]	^{10}Be/^{9}Be × 10^{-14}	[^{10}Be] [× 10^3 at/g]	^{10}Be surface-exposure age [ka]	Snow corrected ^{10}Be surface-exposure age [ka]
VR1	3	0.87	19.61	0.5115	3.12 ± 0.21	55.9 ± 3.7	1.88 ± 0.14 (0.13)	2.04 ± 0.15 (0.14)
VR2	3	0.92	17.79	0.5073	2.19 ± 0.34	41.7 ± 6.5	1.32 ± 0.21 (0.21)	1.43 ± 0.23 (0.23)
VR3	5	0.91	26.18	0.5114	1.09 ± 0.62	142.6 ± 8.1	4.88 ± 0.29 (0.27)	5.25 ± 0.30 (0.28)
VR4	3	0.93	16.12	0.5100	5.02 ± 0.25	105.9 ± 5.3	3.67 ± 0.21 (0.19)	3.96 ± 0.22 (0.20)
VR5	3	0.93	19.01	0.5102	5.36 ± 0.40	96.0 ± 7.2	3.37 ± 0.27 (0.26)	3.63 ± 0.29 (0.28)
VR6	3	0.92	19.74	0.5121	4.70 ± 0.19	81.4 ± 3.4	2.83 ± 0.14 (0.12)	3.07 ± 0.15 (0.13)
VR7	3	0.93	13.29	0.5100	12.85 ± 0.48	32.9 ± 12.3	10.85 ± 0.46 (0.38)	11.64 ± 0.50 (0.42)
VR8	4	0.94	20.50	0.5106	16.12 ± 0.53	267.8 ± 8.9	9.25 ± 0.40 (0.32)	9.99 ± 0.39 (0.32)
VR9	4	0.93	23.10	0.5102	20.83 ± 0.71	306.8 ± 10.4	10.59 ± 0.42 (0.35)	11.37 ± 0.44 (0.36)
VR10	2	0.96	19.72	0.5110	18.50 ± 0.66	319.8 ± 11.5	10.64 ± 0.44 (0.38)	11.44 ± 0.46 (0.38)
VR11	4	0.95	17.48	0.5095	17.46 ± 0.56	339.5 ± 10.9	11.46 ± 0.43 (0.35)	12.37 ± 0.50 (0.40)
VR12	3	0.96	18.34	0.5104	15.25 ± 0.53	283.0 ± 10.0	9.68 ± 0.41 (0.34)	10.43 ± 0.43 (0.35)
VR13	3	0.93	22.29	0.5110	20.15 ± 0.64	308.1 ± 9.9	10.91 ± 0.41 (0.33)	11.71 ± 0.46 (0.37)
VR14	3	0.96	18.04	0.5100	17.71 ± 0.57	333.9 ± 10.8	11.38 ± 0.43 (0.34)	12.28 ± 0.50 (0.40)
VR15	3	0.97	18.81	0.5090	18.11 ± 0.61	326.8 ± 11.1	11.14 ± 0.43 (0.35)	11.98 ± 0.50 (0.41)
VR16	3	0.95	17.26	0.5092	19.03 ± 0.61	374.5 ± 12.2	13.10 ± 0.51 (0.40)	14.09 ± 0.55 (0.44)
VR17	4	0.97	19.76	0.5089	21.44 ± 0.68	368.3 ± 11.8	12.79 ± 0.49 (0.39)	13.75 ± 0.53 (0.42)
VR18	3	0.91	18.78	0.5086	6.05 ± 0.23	109.3 ± 4.2	3.63 ± 0.17 (0.14)	3.92 ± 0.18 (0.15)
VR19	3	0.91	21.18	0.5094	4.78 ± 0.18	76.5 ± 3.0	2.56 ± 0.12 (0.11)	2.76 ± 0.13 (0.11)

Table 3: [10]Be surface-exposure ages for each landform of the rock-glacier system of the Vallon de la Route (Combeynot massif,
France). n represents the number of samples per landform. For the landform with replicates, the median values are reported with
the standard variation ±1σ. For the inheritance estimate, the difference in 10Be concentration of each pair of replicates has been
used and [10]Be surface-exposure ages have been recalculated assuming origin from the headwall (at an elevation of 2997 m a.s.l.).

Landform ID		Corresponding sample	Mean elevation [m a.s.l.]	Mean distance to the headwall [m]	Median ^{10}Be surface-exposure age ±1σ [ka]	Variability [%]	Inheritance est. ±1σ [ka]
A	(n=1)	VR1	2751	246	1.88 ± 0.14		
B	(n=2)	VR18 - VR19	2735	344	3.10 ± 0.76	26	0.88 ± 0.4
C	(n=2)	VR2 - VR3	2728	450	3.10 ± 2.52	99	2.88 ± 0.47
D	(n=1)	VR4	2647	641	3.67 ± 0.21		
E	(n=2)	VR5 - VR6	2646	740	3.10 ± 0.38	13	0.39 ± 0.03
F	(n=1)	VR7	2659	896	10.85 ± 0.46		
G	(n=2)	VR8 - VR9	2606	961	9.92 ± 0.95	10	1.06 ± 0.04
H	(n=1)	VR10	2595	1060	10.64 ± 0.44		
I	(n=1)	VR11	2602	1088	11.46 ± 0.43		
J	(n=2)	VR12 - VR13	2568	1303	10.30 ± 0.87	8	0.67 ± 0.03
K	(n=1)	VR14	2560	1490	11.38 ± 0.43		
L	(n=1)	VR15	2547	1520	11.14 ± 0.43		
M	(n=2)	VR16 - VR17	2534	1715	12.95 ± 0.22	2	0.17 ± 0.01

885 **Table 4: Median value of the [10]Be surface-exposure ages for each unit of the rock-glacier system of the Vallon de la Route (Combeynot massif, France). n represents the number of samples per unit.**

Unit ID		Mean elevation [m a.s.l.]	Mean distance to the headwall [m]	Median [10]Be surface exposure age $\pm 1\sigma$ [ka]	Variability %
Unit I	(n=3)	2740 ± 9	311 ± 58	2.56 ± 0.88	34
Unit II	(n=5)	2679 ± 45	604 ± 147	3.37 ± 1.30	44
Unit III	(n=3)	2624 ± 31	939 ± 38	10.59 ± 0.86	8
Unit IV	(n=4)	2583 ± 19	1189 ± 133	10.78 ± 0.74	7
Unit V	(n=4)	2544 ± 12	1610 ± 122	12.10 ± 0.99	8

890 **Table 5: Surface velocity calculated from [10]Be surface-exposure dating (distance from the headwall divided by [10]Be surface-exposure age) and from image correlation (IMCORR, SAGA package on QGIS) of orthoimages (1960-2018 interval). The median velocities are reported with the standard deviation $\pm 1\sigma$.**

Unit ID	Mean elevation [m a.s.l.]	Mean distance to the headwall [m]	Median [10]Be surface-exposure age [ka]	Median displacement 1960-2018 [m]	Integrated surface velocity [m/a]	
					[10]Be surface-exposure age	1960-2018
Unit I	2740 ± 9	311 ± 58	2.56 ± 0.88	8.08 ± 4.66	0.12 ± 0.06	0.14 ± 0.08
Unit II	2679 ± 45	604 ± 147	3.37 ± 1.30	8.45 ± 2.98	0.18 ± 0.11	0.14 ± 0.05
Unit III	2624 ± 31	939 ± 38	10.59 ± 0.86	1.99 ± 1.50	0.89 ± 0.01	0.03 ± 0.02
Unit IV	2583 ± 19	1189 ± 133	10.78 ± 0.74	0.95 ± 0.55	0.11 ± 0.02	0.01 ± 0.01
Unit V	2544 ± 12	1610 ± 122	12.10 ± 0.99	1.18 ± 0.36	0.13 ± 0.02	0.02 ± 0.01

895

900

905

Earth **Surface**
Dynamics
Discussions

Appendix
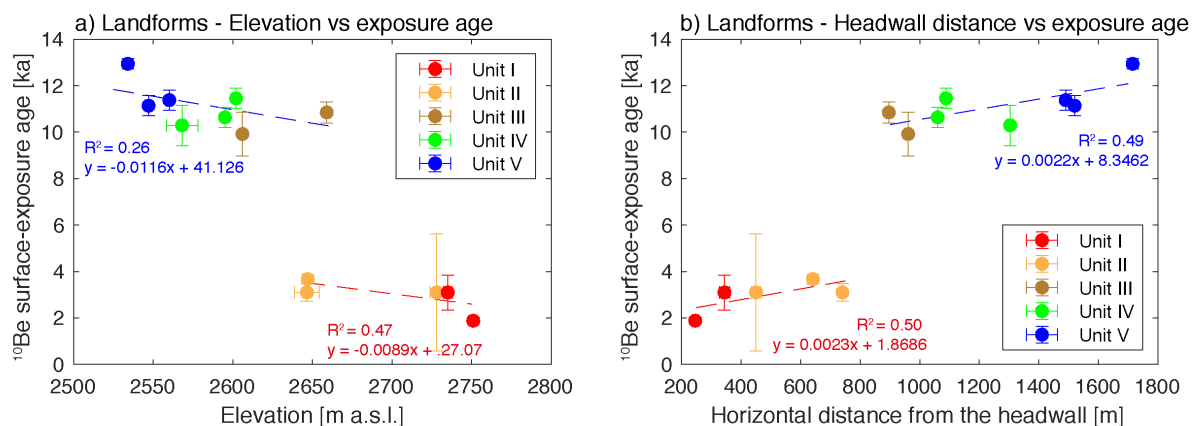
910

Figure A1: ^{10}Be surface-exposure ages of individual landforms (a,b), plotted against elevation (a) and horizontal distance to the headwall (b). The red and blue dashed lines represent the linear regressions for cluster 1 (Units I and II) and 2 (Units III, IV and V), respectively.
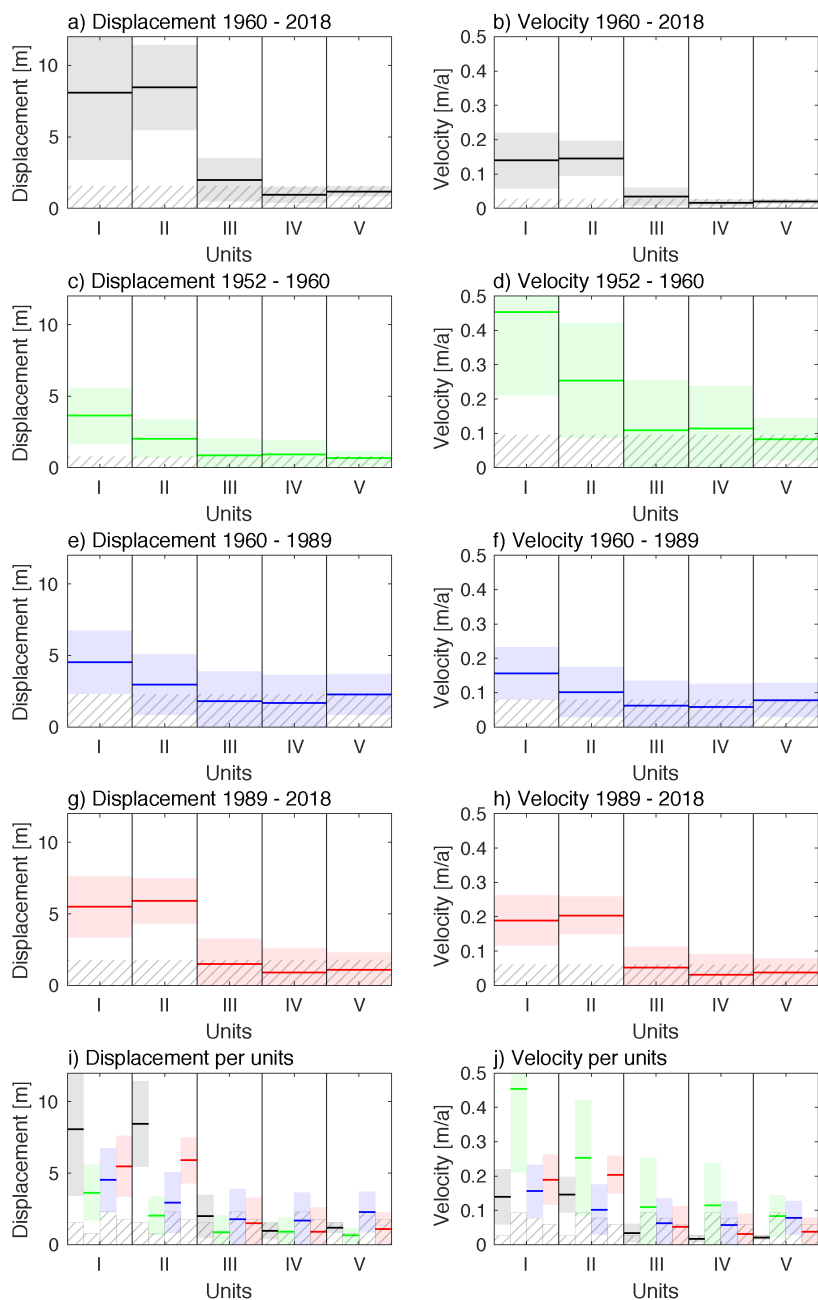
Figure A2: Median surface displacement and velocity for each unit and for every pair of orthoimages tested in this study. Results are presented with the standard deviation ±1σ. The dashed patterns represent the detection limit defined by median value of the control area on Figure 3 used as a threshold value to detect movement.
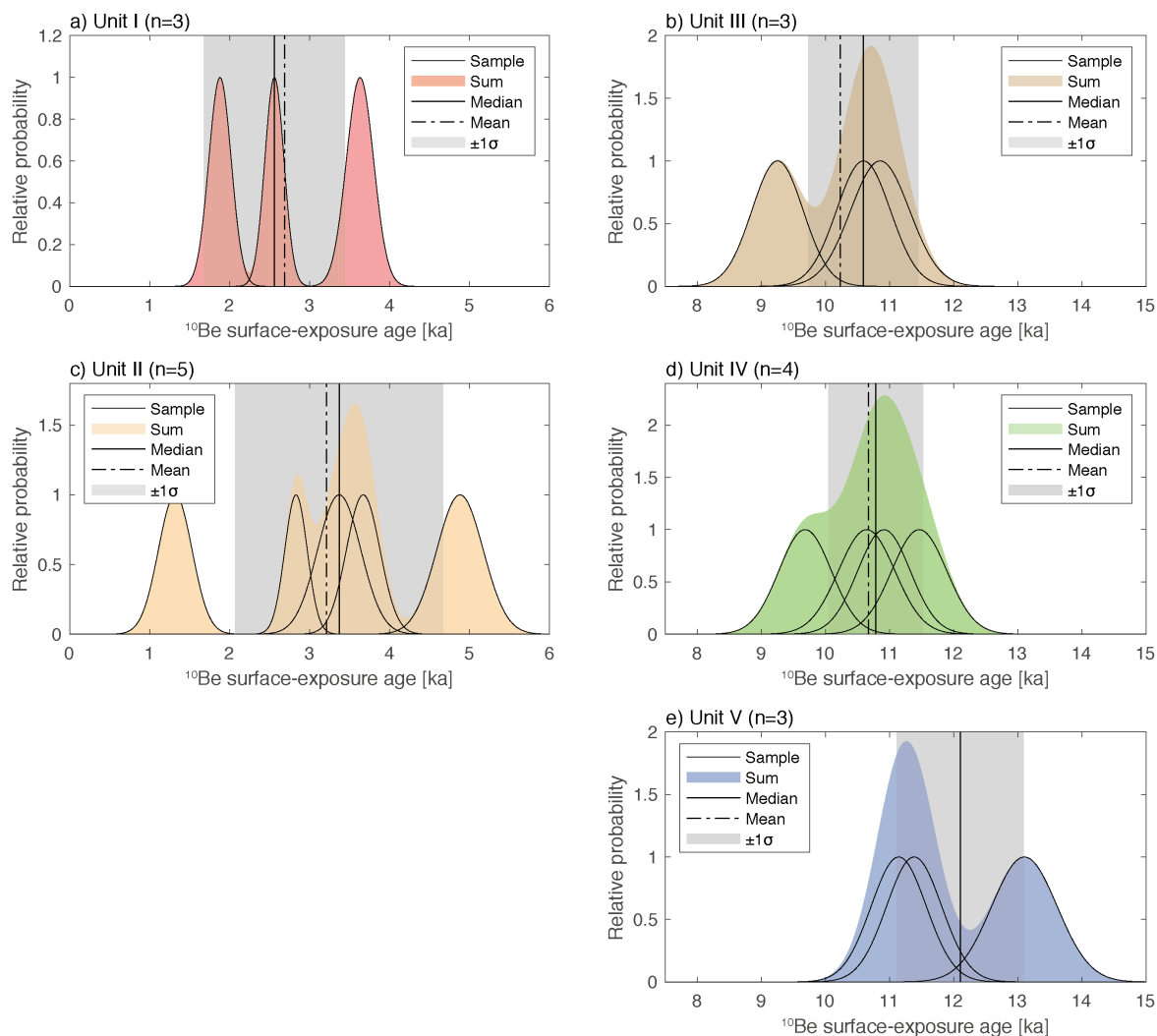
Figure A3: Probability plots of the ^{10}Be surface-exposure ages for individual samples with sum, mean, median and standard deviation for each unit.